Self-Organization and Single-Electron Operation of Group-IV Semiconductor Quantum Dot Structures

A DISSERTATION SUBMITTED TO
THE SCHOOL OF FUNDAMENTAL SCIENCE AND TECHNOLOGY
AND THE COMMITTEE ON GRADUATE STUDIES OF KEIO UNIVERSITY
IN PARTIAL FULFILLMENT OF THE REQUIREMENTS
FOR THE DEGREE OF DOCTOR OF ENGINEERING

Satoru Miyamoto

Principal Adviser

Prof. Kohei M. Itoh	Keio University

Associate Advisers

Prof. Mikio Eto	Keio University
Prof. Toshiharu Saiki	Keio University
Prof. Eiji Ohta	Keio University

Keywords: self-assembled Ge/Si(001) nanoislands, isotopes, Stranski-Krastanov growth mode, type-II quantum dots, excitonic Aharonov-Bohm effect, dynamic quantum dots, silicon nanowire MOSFETs, Brownian ratchet, single-electron transfer, stochastic resonance

Abstract

Possibilities of adding new functions to conventional silicon (Si) semiconductor devices have been extensively explored utilizing quantum effects. Fabrication of high-quality quantum dots on Si substrates and identification of distinct physical effects in such structures hold a key for realization of new functionalities such as quantum information processing and single-electron signal processing. Motivated by these backgrounds, the present thesis describes investigation of self-organization phenomena of Ge-rich quantum dots formed on Si substrates and novel quantum phenomena observed in such nanostructures. Physics associated with Si single-electron devices are also exploited and an essential role of thermal fluctuation and stochastic effect are revealed in the single-electron ejection from a Si quantum dot.

Following the preface of Chapter I, Chapter II describes the growth process of Ge-rich quantum dots on Si surfaces via the Stranski-Krastanov mode. Ge atoms were deposited onto a Si substrate by molecular beam epitaxy. The resulting surface morphology as a function of the number of Ge atomic layers deposited was observed by the atomic force microscope. The effect of Si and Ge atomic diffusion was assessed statistically and the number of atoms required for formation of the critical nuclei was identified. In parallel, the internal composition and strain associated with the quantum dots were determined by Raman spectroscopy probing a specific Ge isotope as a marker. The transport phenomena of Si and Ge atoms among the quantum dots, wetting layer, and underlying substrate were quantitatively evaluated.

Chapter III describes the discovery of oscillatory behaviors of the photoluminescence intensity and energy recorded at temperature 2 K of Ge quantum dots embedded in a Si matrix. The oscillatory behaviors were found to arise from the phase modulation of the electron wave functions by the magnetic flux going through the quantum dots, i.e., due to the Aharonov-Bohm effect.

Chapter IV describes electron ejection behaviors in the Si-based single-electron ratchet transfer device. The ejection process of the first, second, and third electrons from the quantum dot was investigated around 16 K. The characteristic ejection time was found to depend on the number of electrons captured in the quantum dot and the thermal excitation across the barrier was found to be the major cause of the ejection. The accuracy of single-electron ejection was assessed and optimal operation conditions for controlled ejection of a desired number of electrons were found.

Chapter V describes how the single-electron ejection from the Si quantum dot depends on the periodic modulation of the potential barrier that confines the electrons. An enhancement of single-electron ejection was observed when the barrier-modulation period became comparable with the electron ejection time. This corresponded to the first observation of the stochastic resonance in a single-electron system showing that the temporally fluctuated ejection could synchronize with the externally applied modulation.

Finally, summary and future prospects are presented. A description of how the physical phenomena found and understood in the present thesis may contribute to the future development of silicon based nanostructure devices is given.

Acknowledgments

This thesis is the product of an intense collaboration with many people.

First of all, I am very grateful to my principal adviser, Prof. Kohei M. Itoh. This thesis across the wide fields is greatly supported by his broad interest and knowledge. I have benefited from a countlessly large amount of his sincere advice. In addition, I have learned from him how to say the most important things using words as few as possible. I was impressed at his lecture in 2001 when I entered Keio University. It was natural for me to select to join Itoh research group at the department of applied physics and physico-informatics. I was really happy to do research in the excellent environment with many motivated group members including the foreign students.

I would like to cordially thank Dr. Akira Fujiwara, who was my supervisor in nanodevices research group at NTT Basic Research Laboratories. He was willing to agree for me to use the sophisticated devices and environment to my heart's content. His deep insight into the true nature of an occurring phenomenon has always helped my Ph.D. work especially regarding silicon single-electron devices. I would like to thank Prof. Masashi Uematsu at Keio University, who is a former member of this group. He has opened up the exciting opportunity to study in this group. I am very grateful to all the group members, Dr. Katsuhiko Nishiguchi, Dr. Yukinori Ono, Dr. Hiroyuki Kageshima, Dr. Jinichirou Noborisaka, and Dr. Mohammed Khalafalla. Soon after I have joined the group, I could start to carry out research in the atmosphere very at home. I am also grateful to the members of quantum solid state physics research group, Dr. Toshimasa Fujisawa, who is currently a Professor of Tokyo Institute of Technology, and Dr. Takeshi Ota. Although this thesis does not unfortunately include the experimental results employing the dilution refrigerator, the valuable experience occupies a very important part in my research life.

I would like to thank Prof. Eugene E. Haller and Prof. Oscar D. Dubon of

University of California at Berkeley and Lawrence Berkeley National Laboratory (LBNL) for fruitful discussions and careful reading of my manuscripts. The exact calibration of growth rate employing Rutherford backscattering spectroscopy at LBNL allowed the isotope deposition at a submonolayer level in this work.

I am grateful to Prof. Yasuhiro Shiraki and Prof. Kentarou Sawano of Research Center for Silicon Nano-Science at Tokyo City University. The techniques on epitaxial growth in Itoh research group are largely supported by their vast experience and knowledge. With their kindness, I used many refined equipments in their group.

I would like to thank Prof. Yukio Saito, Prof. Mikio Eto, Ryosuke Yoshii, and Rin Okuyama of the physics department at Keio University. The fruitful discussions with them led to further deepen theoretical understandings in the work of Ge/Si quantum dots. I am also grateful to Dr. Bert Voigtländer at Research Center Jülich, who is one of precursors in the field of the Ge growth on Si. His valuable advice was reflected in this work.

Dr. Oussama Moutanabbir was my supervisor when I was in the master's degree program at Keio University. Although we have worked together on the research of isotopically Ge/Si quantum dots only for two years, what I have learned from him was a lot from research to life in general. Even after he has moved to Max Planck Institute of Microstructure Physics, he encouraged me to submit my papers through the intensive discussions. In addition, I would like to thank Dr. Takeharu Sekiguchi. He kindly stayed up late with us for the maintenance of our molecular beam epitaxy machine and the discussion about the growth research. I have learned from him a real attitude as a professional researcher. I am also thankful to the secretary of Itoh research group, Shino Aizawa. Without her clerical supports, my research activities would have not gone well.

I would like to thank Dr. Shigeto Fukatsu, Dr. Eisuke Abe, Dr. Yasuo Shimizu, Shunji Yoshida, and Daisuke Tsurumi. Their enthusiastic attitudes to work on research greatly stimulated me, often leading to stay the lab for difficult and exciting experiments. In particular, their very organized approach I learned from them can be currently applied to everything. Akihiko Sagara and Tomotaka Mouri have always cheered me up when the experiments were not going well. We have really enjoyed

going around Tokyo to eat delicious ramens and the graduate trip to Turkey. It was very nice to share with you the time during my master course. I would like to thank all the members of Itoh research group whom I met during my master and Ph.D. course, Agung Trisetyarso, Hiroki Morishita, Hiroshi Hayashi, Youhei Shiren, Emi Otobe, Mohammad Rizwanur Rahman, Mohammad Waseem Akhtar, Toyofumi Ishikawa, Yoko Kawamura, Kei Yoshizawa, Tatsumasa Itahashi, Shinichi Tojo, Miki Naganawa, Shing-Chiang Huang, Rii Hirano, Go Tsuchiya, Hiroyuki Tezuka, Katsuhiko Naito, Yuri Sakuma, Luis Jou García, Tomoya Arai, Masashi Hirose, Nao Harada, Pierre-Andre Mortemousque, Erika Kawakami, Itaru Arikawa, Michihiro Yamada, Takahisa Tanaka, Takashi Matsuoka, Fangfang Yang, Fumi Yamaga, Akira Fujimoto, Hiroyuki Oshikawa, Makoto Kuroda, and Ken Lee. Thank you all for everything!

For the more practical help, I again acknowledge Akihiko Sagara, Toyofumi Ishikawa, Kei Yoshizawa, Akira Fujimoto, and Hiroyuki Oshikawa. Mainly thanks to Akihiko, I could establish the setup for photoluminescence measurements of Ge/Si quantum dots. It was also very nice to discuss more physical things with Toyofumi. Kei has made contributions to the electronic part of the photoluminescence measurement setup. The beautiful image of transmission electron microscope in this thesis is due to the technical efforts by Akira and Hiroyuki.

Most importantly, I would like to thank my family. Even when I have stayed overnight in the lab, they have prepared my dinner and waited late for me. I am very thankful for all the supports you gave me.

On the financial aspects, this work was supported in part by the Grant-in-Aid for Scientific Research from the Ministry of Education, Culture, Sport, Science, and Technology in Japan (MEXT) (Grant Nos. 18001002, 20241036, and 19310093), in part by Grant-in-Aid for the Global Center of Excellence for High-Level Global Cooperation for Leading-Edge Platform on Access Spaces from MEXT, and in part by Special Coordination Funds for Promoting Science and Technology for Institute for Nano Quantum Information Electronics.

Satoru Miyamoto

February 2010

Contents

Chapter I

Preface

1.1 Recent Progress in Quantum Dots

When a tiny conductive island is charged with a number of electrons, Coulomb repulsive interaction can prevent an extra electron from entering there. This phenomenon known as Coulomb blockade enables precise control of single-electron transport through a semiconductor quantum dot [1]. In 1998, Loss and DiVincenzo proposed a solid-state quantum computing based on electrons confined in quantum dots [2]. Remarkable progress in quantum dot science over the past 10 years has been motivated by intense interest in controlling the degrees of freedom of an individual electron, more specifically charges and spins in quantum dots. Information about charge and spin states can be obtained by spectroscopic measurements of electron transport through single quantum dots [3, 4]. In 2002, Fujisawa *et al.* at NTT Basic Research Laboratories introduced a high-speed electrical pulse technique for the study of their dynamics [5]. The energy relaxation for the spin flip was found to take more than 200 μs, which was four to five orders of magnitude longer than ~ 10 ns of the transition involving only a change in orbital angular momentum. A capacitively coupled quantum point contact was used to detect the occupation of an electron on quantum dots with a single-electron resolution. In 2004, Elzerman *et al.* at Kavli Institute of Nanoscience considered a protocol of spin-to-charge conversion, that allowed for the selective detection of a spin state in single-shot mode [6]. It was shown that the spin relaxation time can be extended up to a second by carefully tuning

orbital confinement and magnetic fields [7].

If we regard a quantum dot as an artificial atom, artificial molecules can be formed by coupling quantum dots in series. A pair of quantum dots (double quantum dot) is used to create a quantum two-level system. Then, the interdot tunnel coupling is electrically varied from a weak coupling regime, where a single electron is localized at one of the pair, to a strong coupling regime, where the electron is delocalized over the pair [8]. The molecular-like coupling of the double quantum dot forms bonding and antibonding states. It has been reported that coherent manipulation of charge states is possible between double quantum dots even though the charge coherence can be lost within a few nanoseconds, for instance, due to background charge fluctuations, cotunneling processes, and electron-phonon interactions [9]. Moreover, the coupling of two electron spins in double quantum dots can form singlet or triplet spin states. When two electrons with parallel spins try to occupy one particular orbital, spin blockade due to the Pauli exclusion principle can occur. Ono *et al.* at University of Tokyo succeeded in observation of this spin blockade in 2002 [10]. The phenomenon of spin blockade provides an effective method for spin-to-charge conversion. In particular, when two electrons are spatially separated by detuning between energy levels in double quantum dots, each electron experiences a slightly different hyperfine field of the host nuclei in the lattice. This difference in the nuclear fields causes strong mixing of the singlet and triplet states. The experimental evidence for this was demonstrated by observation of a current leakage in spin-blockade regions [11,12]. In 2005, Petta *et al.* at Harvard University demonstrated a fast electrical SWAP operation based on the exchange interaction between the single and triplet spin states [13]. In addition, the dephasing effect associated with nuclear spin fluctuations was canceled by applying a simple spin-echo pulse sequence. They found that the characteristic coherence time exceeded 1 μs. More recently, a number of schemes for single-spin rotations in quantum dots were developed in order to implement arbitrary quantum gate operations between two spin states [14,15]. Local electron spin resonance of single spins has been realized in the spin-blockade regime employing an on-chip coplaner stripline [16]. A much simpler method involving electrical shaking of an electron position in the quantum dot was also proposed and demonstrated to effectively generate an oscillating

magnetic field via spin-orbit interactions [17]. Such a fully electrical control through a local gate electrode offers the opportunities for selective spin manipulation.

In parallel, the optical methods have been investigated widely. Self-assembled quantum dots with large oscillator strength of excitonic transitions are needed for fast optical operations. Selective excitation of a single quantum dot has been made possible by lithographically defined apertures on a nanoscale. In 2002, Zrenner *et al.* at Walter Schottky Institute demonstrated the coherent manipulation between two excitonic states and readout by a deterministic current flowing in the Schottky photodiode which contained a large number of InGaAs quantum dots [18]. Stacking of such self-assembled quantum dots separated by thin spacers leads to the strain-driven formation of a vertical quantum dot structure. Indeed, the phenomena corresponding to the molecular-like coupling and the spin blockade have been observed between direct and indirect excitons in electrically controllable double quantum dots [19]. When static electric fields were applied to the photodiode, the quantum confined Stark effect gave rise to a variation in the energy-level separations and charge configuration in double quantum dots. Although the application of a high bias voltage resulted in dissociation of electron and hole pairs, either of the charges could be blocked from escaping out of the quantum dot by inserting an asymmetric barrier above or below the layer. The storage for the optically induced charge carried on over timescales much longer than the excitonic radiative lifetime [20]. If circularly polarized light was illuminated onto such structures, electrons or holes could be selectively stored with well-defined spin states. Conversely, the polarization of photons emitted by the recombination of electron-hole pairs represents the spin orientation of stored charges. Based on this spin to photon polarization conversion, in 2004, Kroutvar *et al.* at the same institute directly measured a very long relaxation time of 20 ms for the optically pumped electron spins [21]. On the other hand, the hole spin lifetime was generally thought to be much shorter than the electron spin lifetime due to the strong spin-orbit mixing in heavy and light hole valence bands. However, the quantum confinement and strain-induced splitting of the subbands reduce the spin-orbit interactions in the quantum dots. Moreover, holes are unlikely to couple with nuclear spins via the contact hyperfine interaction since a p-like wavefunction of holes in the valence band has

zero amplitude at the position of the nuclei. Heiss *et al.* recently reported the observation of extremely long relaxation times up to 300 μs for single hole spins [22]. This result opened up the door to hole-spin-based information processing that would not suffer from the hyperfine-mediated decoherence. Further experiments are necessary to determine the coherence time of the hole spins.

1.2 Group-IV Semiconductor Quantum Dots

The hyperfine interaction with a nuclear spin bath in a host matrix has two major effects on the electron spin. First, the hyperfine interaction leads to electron-spin relaxation via the flip-flop process, in which nuclear spin flipping accompanies electron spin flopping. Secondly, each nuclear spin acts as a source of tiny magnetic field. If $10^5 \sim 10^6$ nuclear spins contained in a GaAs quantum dot are polarized, a magnitude of the nuclear fields known as the Overhauser fields can be several tesla [23, 24]. However, the hyperfine fields in thermal equilibrium slowly fluctuate with an amplitude of a few millitesla at the center of an average field given by the Boltzman distribution [11, 12, 25]. This magnetic-field fluctuation is the dominant source of spin decoherence in the group III-V quantum dots. Unfortunately all stable of III-V systems isotopes possess nonzero nuclear spin. In contrast, group-IV semiconductors such as silicon (Si), germanium (Ge), and carbon (C), are composed primarily by isotopes that are free of nuclear spins. The abundance of a certain isotope having nonzero nuclear spin can be further reduced by isotopic purification. In such nuclear spin-free quantum dots, the coherence time of electron spins should become much longer than those in the group III-V. In addition, the group-IV quantum dots are expected to have long relaxation and coherence times due to the weak spin-orbit interaction and the absence of piezoelectric electron-phonon coupling.

Gate-defined quantum dots are routinely fabricated from a one-dimensional quantum wire or a two-dimensional quantum well. Lateral confinement in the other directions can be achieved by electrical induction of depletion regions underneath patterned

surface gates. For the fabrication of Si quantum dots, a wide variety of processes have been proposed based on the very large scale integrated (VLSI) technology [26, 27]. In particular, Takahashi *et al.* at NTT Basic Research Laboratories have developed a reproducible process called pattern-dependent oxidation (PADOX) and succeeded in the observation of Coulomb-blockade oscillations at room temperature [28]. Moreover, advancement of metal-oxide-semiconductor field-effect transistors (MOSFETs) allowed to demonstrate a highly periodic Coulomb-blockade oscillation and to form double quantum dots with gate-controlled electrostatic barriers [29, 30]. A charge sensing technique has been also integrated to readout the charge occupancy even for a few-electron regime [31]. Thus, the research on group-IV quantum dots is now approaching the level of highly controllable group III-V systems. In fact, the spin blockade phenomenon has been successfully observed in Si double quantum dots similar to the case of GaAs [32]. It is particularly worth noting that a complementary phenomenon of lifetime-enhanced transport arises as a result of a long relaxation time of electron spins [33]. This characteristic has been observed only in Si double quantum dots. For complete suppression of the hyperfine-mediated decoherence of electron spins in Si quantum dots, intensive efforts to realize nuclear-spin-free environments have been made based on isotope engineering [34, 35]. In carbon nanotube double quantum dots, Churchill *et al.* have already reported relaxation and dephasing times of two-electron spins as well as strong isotope effects in spin-blockade transport [36]. The hyperfine coupling strength was found to be greatly enhanced in such one-dimensional structures. These results motivate development of isotopically controlled group-IV quantum dots as an ideal physical system for comprehend the mechanisms of spin relaxation and dephasing.

1.3 Self-Assembled Ge/Si Type-II Quantum Dots

Self-assembled quantum dots are fabricated by the crystal growth of the Stranski-Krastanov (SK) mode [37]. For instance, the deposition of Ge on a Si substrate forms

nanoscale islands as a result of the partial relaxation of strain induced by the 4% difference in the lattice constants [38]. The formation mechanism of self-assembled Ge/Si quantum dots has received considerable attention because these nanostructures are a binary phase model system to highlight complicated strain-driven processes during the SK growth [39].

Such an epitaxial technique is a typical bottom-up approach to obtain small-size and defect-free nanostructures enough to exhibit atomlike and quantum properties [40]. In general, the quantum dot called a type-I structure has a confinement potential for both electron and hole in the bandgap of a surrounding matrix. On the other hand, a type-II quantum dot confines either electron or hole and expels the other type of carriers. Self-assembled Ge/Si quantum dots possess a type-II band alignment; the Ge quantum structures can trap holes while the surrounding Si regions are accumulated with electrons. Due to the spatial separation of the electron and hole, the time required for the optical recombination in type-II quantum dots reaches more than microseconds. Such a slow recombination is expected to occur without losing the spin coherence of electrons. Additionally, the electron-hole separation suppresses the electron spin relaxation via the electron-hole exchange interaction, which is one of the major relaxation mechanisms for electron spins accompanied by the relatively fast hole spin relaxation [41]. Therefore, the Ge/Si quantum dots having type-II structures are desirable for a long-lived spin memory. Furthermore, they are compatible with silicon photonic crystals, which offer an efficient tool to tailor the photon emission rate [42].

1.4 Excitonic Aharonov-Bohm Effects

An important quantum characteristic of electrons is the duality of particle and wave natures. Similar to the Young's double slit experiment, electrons diffracted from double slits in solids show an interference pattern on a screen placed behind. In addition, the application of magnetic fields in the region enclosed by the two paths shifts a phase of the electron wave function. Then, the probability amplitude of detecting electrons at a certain position on the screen is periodically modulated by the applied magnetic fields. Such a topological quantum effect is known as the Aharonov-Bohm

(AB) effect [43]. Conversely, the observation of the AB effect provides evidence that the traveling electrons sufficiently maintain the phase coherence.

In order to observe the AB effect in semiconductors, the magneto-transport experiments of mesoscopic quantum rings has been performed within the magnetic-field range available in today's laboratories [44]. By combining the capacitance and far-infrared absorption spectroscopies, Lorke *et al.* have reported the magnetic-field induced energy modulation in self-assembled quantum rings electrically charged with single electrons [45]. On the other hand, the possibility of the AB effect to occur for neutral composite particles such as an exciton in magnetic fields has been extensively predicted by several theoretical work [46–49]. When there is a difference in effective mass between the electron and hole, each carrier rotates around different trajectories in the quantum ring. Such a radially polarized exciton acquires the relative phase in the presence of the magnetic fields. In fact, the magneto-photoluminescence experiment has demonstrated the AB effect for excitons in InGaAs/GaAs patterned quantum rings [50] and InAs/InP quantum tubes [51]. Similarly, the excitonic AB effects have been reported for InP/GaAs and ZnTe/ZnSe self-assembled type-II quantum dots [52–56]. It was induced by carriers confined in the type-II quantum dot creating ringlike potentials to trap the other type of carriers trapped outside of the quantum dot. To the best of my knowledge, however, no clear AB effect in group-IV semiconductors has been observed probably due to the relatively large effective mass [57]. The self-assembled Ge/Si quantum dots discussed in the present thesis is expected to be nanoscopic enough to exhibit the phase coherence of electrons localized in a silicon.

1.5 Single-Electron Devices

Normally, electrical current involves a large number of electrons, each of which is a carrier of an elementary charge. For instance, one ampere corresponds to a flow of approximately 10^{19} electrons per second. Even though we use a commercially available current meter precise enough to measure down to a fA level, the meter is not sensitive enough to detect the individual electron. From the viewpoints of applica-

tions, quantum dots have been studied as promising candidates for low-power devices because they can deal with single electrons for information processing [27, 58].

In principle, any magnitude of electrical current can be generated by transferring individual elementary charges one by one. When N electrons per one transfer cycle are carried from an upstream electrode to a downstream one, quantized current $I = Nef$ is produced, where f is a repetition frequency. One possible application of single-electron devices is a standard for dc current. Currently, a dc voltage standard is realized by the frequency standard through the Josephson effect. The dc current standard can then be obtained indirectly based on the quantum Hall effect. However, the relationship between the frequency and dc current is the missing side of the quantum metrological triangle linking among the three standards. The realization of the current standards based on the single-electron transfer leads to the completion of this metrological triangle. This provides a test station for evaluating the accuracy of the fundamental physical constants.

The metrological triangle experiment is known to require two stringent criteria; a larger current than a nanoampere level and an extremely high accuracy so that an error does not occurs during the transfer cycle of 10^8 times [59]. A single-electron pump with an error of 15 ppb has been reported for seven metal islands separated by metal-oxide tunnel junctions [60]. The pump device allows to load exactly single electrons onto a nearby cryogenic capacitor and it has been used for building a new standard of capacitance [61]. However, the generated current was in the order of picoampere due to the tunneling rate limit given by the RC constant, where R is the resistance of the tunnel barriers and C the capacitance of the metal island. The tunnel barriers made of metal oxide are fixed in the metal-based devices whereas the gate-tunable barriers available in the semiconductor field have a clear advantage for electrically modulating R during the pumping cycle. When two entrance and exit gate barriers to the quantum dot are lowered alternately, the single-electron transfer becomes possible based on a so-called turnstile operation. This transfer scheme has been demonstrated at the higher frequencies of 20 MHz in GaAs [62] and of 100 MHz in Si [63]. The operation based on the similar method recently reached frequencies up to gigahertz [64]. Meanwhile, another approach for generating a large

current, the usage of surface acoustic waves (SAWs) has been developed [65]. The crystal lattice such as GaAs is periodically deformed via the piezoelectric coupling when a microwave signal is irradiated through an interdigital transducer mounted on the surface. This propagates the dynamic potential waves on the surface and conveys single electrons in one direction. Since the SAWs are usually generated at a frequency within a narrow bandwidth of the interdigital transducer, it is difficult to achieve an arbitrary magnitude of current with preventing microwaves from heating the electron gas.

In the past decade, coherent manipulation between two charge states has been observed in double quantum dots containing many electrons [9]. Single-electron transfer devices can trap and eject an exact number of single electrons. This allows us to observe the coherent motion of charge states in the single-electron regime [66]. In addition, an on-demand single-electron source has been also realized to generate electronic flying qubits in a ballistic conductor [67]. This single-electron technique can be extended to simultaneous control of single electron-hole pairs. Single-photon turnstile devices have been obtained by injecting electrons and holes regularly in a mesoscopic *pn* junction region [68].

1.6 Single-Electron Ratchet Transfer

When particles are trapped at the bottom of an asymmetric potential, unbiased input signals combined with thermal or other noise can drive directed motion of particles even against the gradient of the potential. Since the input energy needed for directed motion is provided by the cyclical modulation of the potential or from a nonequilibrium energy source, the second law of thermodynamics is then kept valid. Such a characteristic phenomenon in asymmetric systems is often called Brownian ratchet, which provides control of quantum particles such as electrons over nanoscale devices [69]. An artificial Brownian ratchet in a mesoscopic region was experimentally verified employing electrons in an asymmetrically modulated potential by Linke *et al.* [70]. It was shown that the direction of ratchet current could be reversed at low temperatures where the quantum-tunneling component governed the nonequilibrium

dynamics. A second example is double quantum dots strongly coupled to a nearby quantum point contact [71]. The quantum point contact at high bias emitted energetic quanta via inelastic relaxation of electrons moving the one-dimensional channel. When the electron energy levels in the two quantum dots were asymmetrically detuned in the linear transport regime, this system drove a net current of electrons. As a matter of course, the notion of Brownian ratchet could be applied to transport electrons in a single-particle unit. Recently, the single-electron ratchet transfer was realized by introducing spatial asymmetry in the system [72, 73]. This attempt consequently reduced the conventional schemes to a single-parameter pumping. Multi-parallelization of such a simplified device has been suggested as a possible solution to achieve a scalable current source [74]. However, the substantial improvement of transfer accuracy is still required for the metrological application. When the number of transferred electron was modulated temporally, a shot noise was imposed on the transfer current. Simultaneous monitoring the shot noise and the transfer current allowed to evaluate the accuracy of the current quantization [75, 76]. These measurements revealed that an error suppression on the quantized plateau was in the order of 10^{-2}. In order to reduce the error rate down to 10^{-8} needed for the current standard, complete understanding of the transfer and error mechanisms is necessary although the dynamics of the single-electron transfer presents a time-dependent many-body problem.

1.7 Stochastic Resonance

Noise is usually considered as a nuisance, which is true in linear systems. In nonlinear systems, however, the presence of noise can in fact help to enhance weak signals. This phenomenon known as stochastic resonance has attracted considerable attention in broad fields from fundamental sciences such as physics, chemistry, and biology to engineering [77].

Originally, the concept of stochastic resonance was proposed as a possible explanation for the ice-age recurrence with an average periodicity of about 10^5 years [78]. The astronomical time scale comparable with such a long-term periodicity is the modula-

tion period of the earth's orbital eccentricity. However, the perturbation only is not strong enough to induce the variation in the solar energy flux on the earth surface. Short-term climate noise such as radiation fluctuations could assist regular transitions between cold glacial and warm interglacial ages. Hence, stochastic resonance is considered as a nonlinear cooperative effect between the periodic perturbation and random fluctuations.

The basic picture of stochastic resonance can be intuitively understood by considering a symmetrical bistable system of a particle switching between two stable states separated by a potential barrier. The relative positions of the potential minima are alternately raised and lowered by a periodic input signal under adiabatic conditions. Even if the signal only is too weak to cause the interwell transition, the inherent or additive noise activates particle hopping in the potential wells, leading them to cross the barrier with a certain probability. The crossing rate given by the Kramers rate depends on the barrier height as well as the noise intensity [79]. At weak noise, the particle rarely switches and continues to stay in one state. Meanwhile, the particle subject to intense noise frequently switches during one period of the input signal. When the switching time is comparable with the half the period of the input signal, the stochastic switching events become synchronized with the deterministic signal. Then, resonance-like behavior of the system response manifests as a function of the noise level.

The most widely used characterization of stochastic resonance is based on the power spectrum of the response signal, which consists of sharp signal peaks at multiples of the driving frequency. With the noise intensity increasing, the signal-to-noise ratio in the power spectrum first increases, passes through a maximum, and then decreases again. Namely, the signal-to-noise ratio can be enhanced by injecting noise at a moderate level so that the incoherent noise power is efficiently transferred to amplify coherent signal components. A first experimental observation of such a characteristic behavior was demonstrated on an electronic circuit of an ac-driven Schmitt trigger by Fauve and Heslot [80]. Five years later, McNamara *et al.* reported an experiment using a bistable ring laser propagating two counter modes [81].

When the driving frequency instead of the noise intensity is tuned, a description

by the signal-to-noise ratio no longer exhibits a resonance-like behavior against the time-scale matching condition for occurrence of stochastic resonance. An alternative approach for emphasizing the synchronization aspect is to characterize the statistical distributions of the residing times during which the particle stays in each state [82]. The residing-time distribution in the absence of the signal decreases exponentially according to the Poissonian statistics. In the presence of the signal, the exponential decay modulated with the same interval as the signal period is observed as a manifestation of the synchronization between the stochastic events and the deterministic signal. The decaying peak heights take a maximum as a function of the noise intensity as well as the driving frequency. Giacomelli *et al.* experimentally established stochastic resonance as a *bona fide* resonance of the coincidence between the stochastic and deterministic time scales [83].

It should be noted that the picture of stochastic resonance is not limited to the bistable systems but can be generalized to simple excitable systems such as integrate-and-fire dynamics and threshold-crossing dynamics. The latter system is a very common model for neuronal dynamics in the presence of periodic stimulus and random noise. When the input exceeds a critical threshold, the neuron fires and then resets itself to the initial zero value. The neuron emits an uncorrelated and sharp spike each time the firing event takes place. The interspike interval histogram is therefore similar to the residing-time distribution for the bistable systems. In terms of both the power spectrum and interspike interval histogram, Moss *et al.* demonstrated stochastic resonance in single neurons of crayfish mechanoreceptors [84]. It was shown that weak signals in neurons can be enhanced by stimulation by noise at an optimal level. In addition, it is interesting that the noise is not necessary to be tuned at the intensity intrinsic to each unit when the neurons having different thresholds form a large network system [85]. In biological systems on a molecular scale, hence, stochastic resonance plays an important role in enhancing the detection efficiency for weak signals and operating robustly against fluctuations.

In modern MOSFET devices, the threshold voltage has been reduced with scaling down towards an atomic level. This technological trend, however, has made the impact of fluctuations on computation accuracy significant [86]. When a billion of such

ultimate transistors are mounted on a silicon, the threshold variation or environmental noise becomes inevitable due to dopant position uncontrollability, atomic-level structural imperfection, interchip crosstalk, thermal fluctuations, and so on. The phenomenon of stochastic resonance provides an idea that such inherent fluctuations should be utilized rather than suppressed. Kasai *et al.* experimentally showed the possibility that the robustness against noise is enhanced in the summing network of MOSFET devices by making use of stochastic resonance [87]. Recently, the state-of-art technology of Si nanofabrication allows us to operate the single-electron devices at high temperature and deal with an electron as a single particle [88]. It was found that the time correlation between the stochastic events for single electrons to surmount the barrier follows the Poissonian statistics. Hence, understanding of the cooperative behavior between noise and signal plays a key role in design and making single-electron devices robust against noise.

1.8 Outline of This Thesis

This thesis describes a self-organization phenomenon of Ge nanostructures formation on a Si substrate and the excitonic Aharonov-Bohm effect in Ge Type-II quantum dot structures (Chapters II and III). Additionally, an essential role of thermal fluctuation in single-electron ratchet transfer and a resonant phenomenon derived from stochastic resonance in the single-electron systems are elucidated in Si quantum dots based on silicon nanowire MOSFETs (Chapters IV and V).

In Chapter II, I address a set of issues in strain-driven self-assembly of the Ge/Si nanostructures, namely:

1. The interaction of the self-assembled nanoislands with their local environment;
2. The experimental determination of the critical size of the nuclei that are precursors of the following nanoisland growth;
3. The evolution of the strain and composition during the growth process.

The dynamic interaction of the growing islands with their local environment is investigated based on a statistical analysis using atomic force microscope and Voronoi tessellation (Wigner-Seitz cell). In addition, Raman scattering is employed to deter-

mine the evolution of the composition and strain during the growth. An isotopically purified ^{76}Ge source is used for the growth, which allows me to extract subtle details in Ge/Si nanoisland at the early stage of the growth. A stabilizing role of substrate atoms and surface imperfections is suggested as an explanation of the relatively small critical sizes of the precursors of nanoislands. I reveal strong atomic diffusion during the nucleation and growth processes.

In Chapter III, I demonstrate the experimental observation of the excitonic AB effect in the self-assembled Ge/Si type-II quantum dots. The quantum structures investigated in this Chapter are grown from an isotopically purified ^{70}Ge source possessing zero nuclear spins. The clear AB oscillations in the magneto-photoluminescence properties are shown due to the change in the angular momentum of the electron circulating around the quantum dot. I provide the evidence of the phase coherence for the electron wave function localized in a silicon.

In Chapter IV, I present the transfer dynamics of a few electrons in the single-electron ratchet based on silicon nanowire MOSFETs. Time-resolved measurements are carried out to determine the escape times from the quantum dot. It is shown that the escape dynamics within the temperature range investigated is described by the thermal activation rather than quantum-tunneling process. I discuss the accuracy of single-electron ejection in the single-electron ratchet.

In Chapter V, I investigate a universal problem of single-electron escape from a potential well over an oscillating barrier. The use of silicon-based single-electron ratchet transfer devices allows the trapping of a single electron as a classical particle. It is shown that the single-electron escape is resonantly driven when the barrier is periodically oscillating on a time scale characteristic of the stochastic escape process itself. I present the experimental observation of the stochastic resonance of single electrons.

Finally, summary is described together with future prospects.

References

[1] For a review see, U. Meirav and E. B. Foxman, Semicond. Sci. Technol. **11**, 255 (1996).

[2] D. Loss and D. P. DiVincenzo, Phys. Rev. A **57**, 120 (1998).

[3] R. C. Ashoori, Nature (London) **379**, 413 (1996).

[4] L. Kouwenhoven and C. Marcus, Phys. World **11**, 35 (1998); L. P. Kouwenhoven, D. G. Austing, and S. Tarucha, Rep. Prog. Phys. **64**, 701 (2001).

[5] T. Fujisawa, D. G. Austing, Y. Tokura, Y. Hirayama, and S. Tarucha, Nature (London) **419**, 278 (2002); T. Fujisawa, D. G. Austing, Y. Tokura, Y. Hirayama, and S. Tarucha, J. Phys.: Condens. Matter **15**, R1395 (2003); T. Fujisawa, T. Hayashi, and S. Sasaki, Rep. Prog. Phys. **69**, 759 (2006).

[6] J. M. Elzerman, R. Hanson, L. H. Willems van Beveren, B. Witkamp, L. M. K. Vandersypen, and L. P. Kouwenhoven, Nature (London) **430**, 431 (2004).

[7] S. Amasha, K. MacLean, I. P. Radu, D. M. Zumbühl, M. A. Kastner, M. P. Hanson, and A. C. Gossard, Phys. Rev. Lett. **100**, 046803 (2008).

[8] W. G. van der Wiel, S. De Franceschi, J. M. Elzerman, T. Fujisawa, S. Tarucha, and L. P. Kouwenhoven, Rev. Mod. Phys. **75**, 1 (2003).

[9] T. Hayashi, T. Fujisawa, H. D. Cheong, Y. H. Jeong, and Y. Hirayama, Phys. Rev. Lett. **91**, 226804 (2003).

[10] K. Ono, D. G. Austing, Y. Tokura, and S. Tarucha, Science **297**, 1313 (2002).

[11] A. C. Johnson, J. R. Petta, J. M. Taylor, A. Yacoby, M. D. Lukin, C. M. Marcus, M. P. Hanson, and A. C. Gossard, Nature (London) **435**, 925 (2005).

[12] F. H. L. Koppens, J. A. Folk, J. M. Elzerman, R. Hanson, L. H. Willems van Beveren, I. T. Vink, H. P. Tranitz, W. Wegscheider, L. P. Kouwenhoven, and L. M. K. Vandersypen, Science **309**, 1346 (2005).

[13] J. R. Petta, A. C. Johnson, J. M. Taylor, E. A. Laird, A. Yacoby, M. D. Lukin, C. M. Marcus, M. P. Hanson, and A. C. Gossard, Science **309**, 2180 (2005).

[14] R. Hanson, L. P. Kouwenhoven, J. R. Petta, S. Tarucha, L. M. K. Vandersypen, Rev. Mod. Phys. **79**, 1217 (2007).

[15] R. Hanson and D. D. Awschalom, Nature (London) **453**, 1043 (2008).

[16] F. H. L. Koppens, C. Buizert, K. J. Tielrooij, I. T. Vink, K. C. Nowack, T. Meunier, L. P. Kouwenhoven, and L. M. K. Vandersypen, Nature (London) **442**, 766 (2006).

[17] K. C. Nowack, F. H. L. Koppens, Y. V. Nazarov, and L. M. K. Vandersypen, Science **318**, 1430 (2007).

[18] A. Zrenner, E. Beham, S. Stufler, F. Findeis, M. Bichler, and G. Abstreiter, Nature (London) **418**, 612 (2002).

[19] H. J. Krenner, M. Sabathil, E. C. Clark, A. Kress, D. Schuh, M. Bichler, G. Abstreiter, and J. J. Finley, Phys. Rev. Lett. **94**, 057402 (2005); H. J. Krenner, E. C. Clark, T. Nakaoka, M. Bichler, C. Scheurer, G. Abstreiter, and J. J. Finley, *ibid.* **97**, 076403 (2006); H. J. Krenner, S. Stufler, M. Sabathil, E. C. Clark, P. Ester, M. Bichler, G. Abstreiter, J. J. Finley, and A. Zrenner, New J. Phys. **7**, 184 (2005).

[20] M. Kroutvar, Y. Ducommun, J. J. Finley, M. Bichler, G. Abstreiter, and A. Zrenner, Appl. Phys. Lett. **83**, 443 (2003); D. Heiss, V. Jovanov, M. Caesar, M. Bichler, G. Abstreiter, and J. J. Finley, Appl. Phys. Lett. **94**, 072108 (2009).

[21] M. Kroutvar, Y. Ducommun, D. Heiss, M. Bichler, D. Schuh, G. Abstreiter, and J. J. Finley, Nature (London) **432**, 81 (2004).

[22] D. Heiss, S. Schaeck, H. Huebl, M. Bichler, G. Abstreiter, J. J. Finley, D. V. Bulaev, and D. Loss, Phys. Rev. B **76**, 241306(R) (2007).

[23] J. Baugh, Y. Kitamura, K. Ono, and S. Tarucha, Phys. Rev. Lett. **99**, 096804 (2007).

[24] A. S. Bracker, E. A. Stinaff, D. Gammon, M. E. Ware, J. G. Tischler, A. Shabaev, Al. L. Efros, D. Park, D. Gershoni, V. L. Korenev, and I. A. Merkulov, Phys. Rev. Lett. **94**, 047402 (2005).

[25] P.-F. Braun, X. Marie, L. Lombez, B. Urbaszek, T. Amand, P. Renucci, V. K. Kalevich, K. V. Kavokin, O. Krebs, P. Voisin, and Y. Masumoto, Phys. Rev. Lett. **94**, 116601 (2005).

[26] M. A. Kastner, Rev. Mod. Phys. **64**, 849 (1992).

[27] Y. Takahashi, Y. Ono, A. Fujiwara, and H. Inokawa, J. Phys.: Condens. Matter **14**, R995 (2002); Y. Ono, A. Fujiwara, K. Nishiguchi, H. Inokawa, and Y. Takahashi, J. Appl. Phys. **97**, 031101 (2005).

[28] Y. Takahashi, M. Nagase, H. Namatsu, K. Kurihara, K. Iwdate, Y. Nakajima, S. Horiguchi, K. Murase, and M. Tabe, Electron. Lett. **31**, 136 (1995).

[29] A. Fujiwara, H. Inokawa, K. Yamazaki, H. Namatsu, Y. Takahashi, N. M. Zimmerman, and S. B. Martin, Appl. Phys. Lett. **88**, 053121 (2006).

[30] W. H. Lim, H. Huebl, L. H. Willems van Beveren, S. Rubanov, P. G. Spizzirri, S. J. Angus, R. G. Clark, and A. S. Dzurak, Appl. Phys. Lett. **94**, 173502 (2009).

[31] Y. Hu, H. O. H. Churchill, D. J. Reilly, J. Xiang, C. M. Lieber, and C. M. Marcus.

Nature Nanotech. **2**, 622 (2007).

[32] H. W. Liu, T. Fujisawa, Y. Ono, H. Inokawa, A. Fujiwara, K. Takashina, and Y. Hirayama, Phys. Rev. B **77**, 073310 (2008).

[33] N. Shaji, C. B. Simmons, M. Thalakulam, L. J. Klein, H. Qin, H. Luo, D. E. Savage, M. G. Lagally, A. J. Rimberg, R. Joynt, M. Friesen, R. H. Blick, S. N. Coppersmith, and M. A. Eriksson, Nature Phys. **4**, 540 (2008).

[34] J. Sailer, V. Lang, G. Abstreiter, G. Tsuchiya, K. M. Itoh, J. W. Ager III, E. E. Haller, D. Kupidura, D. Harbusch, S. Ludwig, and D. Bougeard, Phys. Status Solidi RRL **3**, 61 (2009).

[35] O. Moutanabbir, S. Senz, Z. Zhang, and U. Gösele, Nano Today **4**, 393 (2009).

[36] H. O. H. Churchill, A. J. Bestwick, J. W. Harlow, F. Kuemmeth, D. Marcos, C. H. Stwertka, S. K. Watson, and C. M. Marcus, Nature Phys. **5**, 321 (2009); H. O. H. Churchill, F. Kuemmeth, J. W. Harlow, A. J. Bestwick, E. I. Rashba, K. Flensberg, C. H. Stwertka, T. Taychatanapat, S. K. Watson, and C. M. Marcus, Phys. Rev. Lett. **102**, 166802 (2009).

[37] I. N. Stranski and L. Krastanow, Sitzungsber. Akad. Wiss. Wien, Math.-Naturwiss. Kl., Abt. 2B **146**, 797 (1938).

[38] Y.-W. Mo, D. E. Savage, B. S. Swartzentruber, and M. G. Lagally, Phys. Rev. Lett. **65**, 1020 (1990).

[39] For a review see, B. Voigtländer, Surf. Sci. Rep. **43**, 127 (2001); K. Brunner, Rep. Prog. Phys. **65**, 27 (2002); J. Stangl, V. Holý, and G. Bauer, Rev. Mod. Phys. **76**, 725 (2004).

[40] P. M. Petroff, A. Lorke, and A. Imamoglu, Phys. Today **54(5)**, 46 (2001).

[41] H. Mino, Y. Kouno, K. Oto, K. Muro, R. Akimoto, and S. Takeyama, Appl. Phys. Lett. **92**, 153101 (2008).

[42] J. S. Xia, Y. Ikegami, Y. Shiraki, N. Usami, and Y. Nakata, Appl. Phys. Lett. **89**, 201102 (2006).

[43] Y. Aharonov and D. Bohm, Phys. Rev. **115**, 485 (1959).

[44] A. Fuhrer, S. Lüscher, T. Ihn, T. Heinzel, K. Ensslin, W. Wegscheider, and M. Bichler, Nature (London) **413**, 822 (2001).

[45] A. Lorke, R. J. Luyken, A. O. Govorov, J. P. Kotthaus, J. M. Garcia, and P. M. Petroff, Phys. Rev. Lett. **84**, 2223 (2000).

[46] A. V. Chaplik, JETP Lett. **62**, 900 (1995).

[47] A. B. Kalameitsev, V. M. Kovalev, and A. O. Govorov, JETP Lett. **68**, 669 (1998).

[48] K. L. Janssens, B. Partoens, and F. M. Peeters, Phys. Rev. B **64**, 155324 (2001).

[49] A. O. Govorov, S. E. Ulloa, K. Karrai, and R. J. Warburton, Phys. Rev. B **66**, 081309(R) (2002).

[50] M. Bayer, M. Korkusinski, P. Hawrylak, T. Gutbrod, M. Michel, and A. Forchel, Phys. Rev. Lett. **90**, 186801 (2003).

[51] K. Tsumura, S. Nomura, P. Mohan, J. Motohisa, and T. Fukui, Jpn. J. Appl. Phys. **46**, L440 (2007).

[52] E. Ribeiro, A. O. Govorov, W. Carvalho, Jr., and G. Medeiros-Ribeiro, Phys. Rev. Lett. **92**, 126402 (2004).

[53] M. H. Degani, M. Z. Maialle, G. Medeiros-Ribeiro, and E. Ribeiro, Phys. Rev. B **78**, 075322 (2008).

[54] I. L. Kuskovsky, W. MacDonald, A. O. Govorov, L. Mourokh, X. Wei, M. C. Tamargo, M. Tadic, and F. M. Peeters, Phys. Rev. B **76**, 035342 (2007).

[55] I. R. Sellers, V. R. Whiteside, I. L. Kuskovsky, A. O. Govorov, and B. D. McCombe, Phys. Rev. Lett. **100**, 136405 (2008).

[56] I. R. Sellers, V. R. Whiteside, A. O. Govorov, W. C. Fan, W-C. Chou, I. Khan, A. Petrou, and B. D. McCombe, Phys. Rev. B **77**, 241302(R) (2008).

[57] W. X. Gao, K. Ismail, K. Y. Lee, J. O. Chu, and S. Washburn, Appl. Phys. Lett. **65**, 3114 (1994).

[58] K. K. Likharev, Proc. IEEE **87**, 606 (1999).

[59] R. E. Elmquist, N. M. Zimmerman, and W. H. Huber, IEEE Trans. Instrum. Meas. **52**, 590 (2003).

[60] M. W. Keller, J. M. Martinis, N. M. Zimmerman, and A. H. Steinbach, Appl. Phys. Lett. **69**, 1804 (1996).

[61] M. W. Keller, A. L. Eichenberger, J. M. Martinis, and N. M. Zimmerman, Science **285**, 1706 (1999).

[62] L. P. Kouwenhoven, A. T. Johnson, N. C. van der Vaart, C. J. P. M. Harmans, and C. T. Foxon, Phys. Rev. Lett. **67**, 1626 (1991).

[63] A. Fujiwara, N. M. Zimmerman, Y. Ono and Y. Takahashi, Appl. Phys. Lett. **84**, 1323 (2004).

[64] M. D. Blumenthal, B. Kaestner, L. Li, S. Giblin, T. J. B. M. Janssen, M. Pepper, D. Anderson, G. Jones, and D. A. Ritchie, Nature Phys. **3**, 343 (2007).

[65] J. M. Shilton, V. I. Talyanskii, M. Pepper, D. A. Ritchie, J. E. F. Frost, C. J. B. Ford, C. G. Smith, and G. A. C. Jones, J. Phys.: Condens. Matter **8**, L531 (1996).

[66] M. Kataoka, M. R. Astley, A. L. Thorn, D. K. L. Oi, C. H. W. Barnes, C. J. B. Ford, D. Anderson, G. A. C. Jones, I. Farrer, D. A. Ritchie, and M. Pepper, Phys. Rev. Lett. **102**, 156801 (2009).

[67] F. Fève, A. Mahé, J.-M. Berroir, T. Kontos, B. Plaçais, D. C. Glattli, A. Cavanna, B. Etienne, and Y. Jin, Science **316**, 1169 (2007).

[68] J. Kim, O. Benson, H. Kan, and Y. Yamamoto, Nature (London) **397**, 500 (1999).

[69] For a review see, P. Reimann, Phys. Rep. **361**, 57 (2002); R. D. Astumian and P. Hänggi, Phys. Today **55(11)**, 33 (2002); P. Hänggi and F. Marchesoni, Rev. Mod. Phys. **81**, 387 (2009).

[70] H. Linke, T. E. Humphrey, A. Löfgren, A. O. Sushkov, R. Newbury, R. P. Taylor, and P. Omling, Science **286**, 2314 (1999).

[71] V. S. Khrapai, S. Ludwig, J. P. Kotthaus, H. P. Tranitz, and W. Wegscheider, Phys. Rev. Lett. **97**, 176803 (2006).

[72] A. Fujiwara, K. Nishiguchi, and Y. Ono, Appl. Phys. Lett. **92**, 042102 (2008).

[73] B. Kaestner, V. Kashcheyevs, S. Amakawa, M. D. Blumenthal, L. Li, T. J. B. M. Janssen, G. Hein, K. Pierz, T. Weimann, U. Siegner, and H. W. Schumacher, Phys. Rev. B **77**, 153301 (2008).

[74] S. J. Wright, M. D. Blumenthal, M. Pepper, D. Anderson, G. A. C. Jones, C. A. Nicoll, and D. A. Ritchie, Phys. Rev. B **80**, 113303 (2009).

[75] A. M. Robinson and V. I. Talyanskii, Phys. Rev. Lett. **95**, 247202 (2005).

[76] N. Maire, F. Hohls, B. Kaestner, K. Pierz, H. W. Schumacher, and R. J. Haug, Appl. Phys. Lett. **92**, 082112 (2008).

[77] For a review, see K. Wiesenfeld and F. Moss, Nature (London) **373**, 33 (1995); A. R. Bulsara and L. Gammaitoni, Phys. Today **49**(3), 39 (1996); L. Gammaitoni, P. Hänggi, P. Jung, and F. Marchesoni, Rev. Mod. Phys. **70**, 223 (1998).

[78] R. Benzi, A. Sutera, and A. Vulpiani, J. Phys. A **14**, L453 (1981).

[79] P. Hänggi, P. Talkner, and M. Borkovec, Rev. Mod. Phys. **62**, 251 (1990).

[80] S. Fauve and F. Heslot, Phys. Lett. A **97**, 5 (1983).

[81] B. McNamara, K. Wiesenfeld, and R. Roy, Phys. Rev. Lett. **60**, 2626 (1988); B. McNamara and K. Wiesenfeld, Phys. Rev. A **39**, 4854 (1989).

[82] L. Gammaitoni, F. Marchesoni, and S. Santucci, Phys. Rev. Lett. **74**, 1052 (1995).

[83] G. Giacomelli, F. Marin, and I. Rabbiosi, Phys. Rev. Lett. **82**, 675 (1999).

[84] J. K. Douglass, L. Wilkens, E. Pantazelou, and F. Moss, Nature (London) **365**, 337 (1993).

[85] J. J. Collins, C. C. Chow, and T. T. Imhoff, Nature (London) **376**, 236 (1995).

[86] L. Gammaitoni, Appl. Phys. Lett. **91**, 224104 (2007).

[87] S. Kasai and T. Asai, Appl. Phys. Express **1**, 083001 (2008).

[88] K. Nishiguchi, Y. Ono, A. Fujiwara, H. Inokawa, and Y. Takahashi, Appl. Phys. Lett. **92**, 062105 (2008).

Chapter II

Spatial Correlation of Isotopically Pure Ge/Si(001) Nanoislands

By using a statistical method based on Voronoi tessellation, we investigated the nucleation of strain-driven self-assembled Ge/Si(001) nanoislands and their dynamic interaction with the local environment. The evolution of the composition and strain during the growth process was also studied by Raman scattering. The use of isotopically purified ^{76}Ge source allows the observation of faint features in the 3D nanoisland Raman signal at the early stage of the growth. The nucleus critical sizes are deduced from the scaling behavior of the Voronoi cell areas and the grown island volumes. The relatively small critical size suggests a stabilizing role of Si atoms and surface imperfections. Additionally, we found that the nucleation process on the metastable 2D layer cannot only be described by the capture of newly deposited Ge atoms, but it is strongly governed by the diffusive interaction with the SiGe alloyed layer.

This Chapter has been published in Physical Review B **79**, 165415 (2009).

2.1 Introduction

Strain-mediated self-assembly is a versatile process by which a variety of quantum and nanoscale structures can be obtained providing a wide spectrum of potential applications in nanoelectronics, optoelectronics, and quantum information [1]. In the case of small lattice mismatched heteroepitaxy, the formation of nanostructures is governed by the Stranski-Krastanow (SK) growth mode [2]. This growth mode is characterized by the transition from two-dimensional (2D) layer-by-layer growth to three-dimensional (3D) islanding which occurs beyond a critical thickness of a few atomic layers to relieve the compressive strain. At the atomic scale, the nucleation process is triggered by the interaction of deposited adatom with other adatoms or surface defects resulting in stable nuclei. These nuclei grow to mature 3D islands by capturing more atoms. The quantitative description of the atomic transport during the nucleation and growth remains a formidable challenge. For its simplicity, Ge deposition on Si has attracted a great deal of attention as a model system to explore the subtle details in SK growth and to investigate the underlying physics of strain-driven nucleation. At relatively low temperatures ($T < 600$ °C), only hut clusters bounded by {105} facets are formed due to the kinetic restrictions [3]. In contrast, coherent islands with steeper well-defined facets such as square-based pyramids or round-based domes are formed at temperatures above 600 °C [4]. Si-Ge intermixing in self-assembled nanostructure leads to the smearing out of the atom-like potential well expected for a pure Ge quantum dot [5]. This phenomenon is unavoidable and occurs at the early stage of the Ge deposition on the Si substrate [6, 7].

In this Chapter, the nucleation and growth of 3D islands on the alloyed 2D layer are investigated at the growth temperature $T = 620$ °C. At this temperature, both kinetics and thermodynamics play competitive roles. In our study, we combine the geometrical assessment with the composition and strain characterization to trace the nucleation and growth processes from the nuclei to the 3D islands. Beyond the critical thickness, the nuclei greater than a critical size are generated on the 2D layer. The nucleation process increases the fraction of the surface area covered with the diffusion

cells corresponding to circles with a radius equal the diffusion length centered on the nucleus. The adatoms within the diffusion cells contribute to the growth of the existing stable nuclei and those outside aggregate, leading to the generation of nuclei. When the entire surface is fully covered by ensembles of diffusion cells, most of the adatoms can steadily participate in the growth of the islands. The capture zone model is introduced to describe the competition among the coexisting islands to capture the deposited adatoms. This simple model can be investigated with the help of the Voronoi cell (Wigner-Seitz cell), which is defined as the region enclosed by the perpendicular bisectors between the centers of the nearest neighboring islands [8–10]. The intersection between the Voronoi cell and the diffusion cell gives the capture zone associated with each island. This allows us to analyze the tendency of adatoms to be incorporated into the closest island. Based on this geometrical correlation between the Voronoi cells and the resulting 3D islands, we show that the growth of 3D islands involves not only Ge atoms evaporated on the wetting layer but also Si and Ge atoms transported from the SiGe alloy wetting layer, the underlying substrate, and probably the neighboring strained islands. The scaling analyses of the grown island volumes and the Voronoi cell areas experimentally determine the critical size of nuclei leading to pyramids and domes. In addition, our analysis contributes to elucidate the evolution of the 3D islands in their coexisting states. Each nucleus grows rather independently from others, eroding the intermixed wetting layer surrounding them. When the distance to the nearest neighbor becomes significantly small, the smaller pyramids act as precursors for material redistribution towards the adjacent larger domes. Such strong material-mediated interactions among the intermixed wetting layer and the neighboring islands of different sizes were reported previously based on the experimental observation of wetting layer consumption [11–13] and anomalous coarsening [14,15]. However, the composition within the grown islands and the role of strain on the intra-island interaction are still debated [16–19]. Therefore, we employ Raman scattering spectroscopy to provide a comprehensive and quantitative overview of the mass interactions during nucleation and growth of 3D islands.

2.2 Experimental Details

The Ge island growth was performed on a p-type Si(001) substrate using solid source molecular beam epitaxy (MBE). Before being introduced into the chamber, the substrate was chemically cleaned by the Ishizaka-Shiraki method [20]. The protective oxide film was removed in the growth chamber by annealing the substrate at 800 °C. The surface cleanliness, especially *regarding carbon*, was confirmed by the (2 × 1) streaky pattern of reflection high-energy electron diffraction. After the cleaning process the temperature was gradually reduced to $T = 620$ °C for Ge deposition. Ge was deposited onto the substrate from an isotopically purified ^{76}Ge solid source heated at 1160 °C in an effusion cell. The pressure in the chamber during the growth was kept in the range of 10^{-10} Torr. Here the deposition rate of ^{76}Ge was fixed at 0.04 ML/s (1.0 ML = 6.78×10^{14} atoms/cm^2). The growth rate was determined using Rutherford backscattering spectrometry. The substrate was cooled down to room temperature immediately after the growth. The surface morphology was investigated by *ex situ* atomic force microscope (AFM) in tapping mode. The critical thickness of 2D-3D transition, WL, was defined as the maximum Ge coverage at which no 3D islands were observed by AFM. Under our growth conditions, this thickness is found to be WL = 4.4 ± 0.1 ML. The aim of the present Chapter is the investigation of the nucleation and growth of self-assembled Ge islands on the 2D layer. Therefore, the "zeroth monolayer," the starting point, is defined as the point at which the wetting layer is completed. This means, for example, that 1.0 ML growth from now on refers to the growth of a 4.4 ML wetting layer followed by a 1.0 ML deposition that induces the 3D islanding via the SK mode. Micro-Raman scattering spectroscopy was carried out at room temperature using Ar^+ 514.5 nm laser focused to a 1-μm-diameter spot. The backscattered light was dispersed by a single spectrometer and detected by a charge coupled device. The spectral distance between adjacent channels is 0.7 cm^{-1}.

2.3 Statistical Assessment using Voronoi Cell Analysis

The correlation between the volume of the grown 3D island and the corresponding Voronoi cell areas is an important index to reveal the dynamic behaviors of adatoms on the 2D layer. If the correlation coefficient is close to unity, the capture zone model would turn out to be valid, indicating that the adatoms on the surface would tend to be incorporated into the nearest neighboring islands [9]. The insets in Fig. 2.1 display AFM images of samples obtained upon deposition of 0.2, 0.8, and 2.0 ML. The types of the observed islands are identified to be square-based pyramids and round-based domes. The network superimposed on AFM images shows the Voronoi tessellation calculated from the center of each island. Figure 2.1 shows the distribution of the volume of the 3D islands as a function of the corresponding Voronoi cell areas by evaluation of 500 islands at given amount of Ge deposited on the 2D layer. The 3D islands are clearly separated into two groups corresponding to small pyramids and relatively large domes by the boundary set at the critical volume of $V_c = 1.2 \times 10^4$ nm^3. The validity of the capture zone model in the deposition range of 0.2–4.0 ML is statistically analyzed by the correlation coefficient r [Fig. 2.2(a)]. The evolution of the island density is also an important parameter projecting the nucleation frequency [Fig. 2.2(b)]. By assuming the validity of the capture zone model, the nucleation process can be described as follows [21]: Initially the number of nuclei is so small that the wetting layer surface cannot be covered completely with the diffusion cells. This manifests as a poor correlation because of the break of the Voronoi cell approximation for the capture zone. Then the adatoms within the diffusion cells can be gathered into the stable nuclei whereas the continuous nucleation outside promotes the branching of the Voronoi boundaries. The correlation coefficient is improved due to the exclusive generation of nuclei until 3D island density stops increasing. When the diffusion cells overlap with each other, most of adatoms can contribute to the growth of 3D islands instead of nucleation at the steady-state regime. Beyond 1.0 ML, the Voronoi cell areas converge at the vertical broken line in Fig. 2.1. At this regime, the correlation

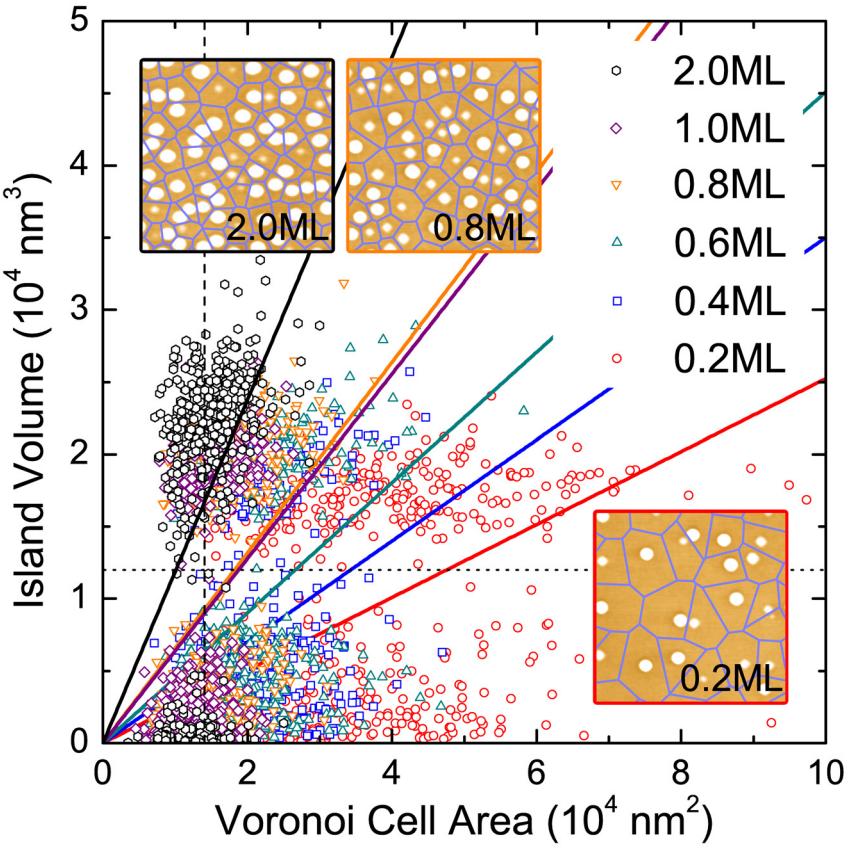

Figure 2.1: Distributions of the island volumes as a function of the corresponding Voronoi cell areas at 0.2, 0.4, 0.6, 0.8, 1.0, and 2.0 ML. The insets display AFM images (1 μm $\times$ 1 μm) for the Ge deposition of 0.2, 0.8, and 2.0 ML. Distinction between pyramids and domes is made by analyzing the island facets. The network superimposed on AFM images shows the Voronoi tessellation calculated from the center of each island. The horizontal dotted line shows the critical volume of $V_c = 1.2 \times 10^4$ nm^3 separating between small pyramids and large domes. The solid lines are the best linear fits to obtain the correlation coefficients. The vertical broken line denotes the average Voronoi cell area at the steady-state regime.

coefficient should approach unity as the Voronoi cells would coincide with the diffusion cells. However, it takes a value far below unity, as shown in Fig. 2.2(a), implying that the growth of 3D islands involves more complex processes than this simple model that considers the deposited Ge adatoms as the unique source of material. More specifically, the intermixed wetting layer and the underlying substrate in the vicinity of islands must be taken into account as material resources. It is worth pointing out

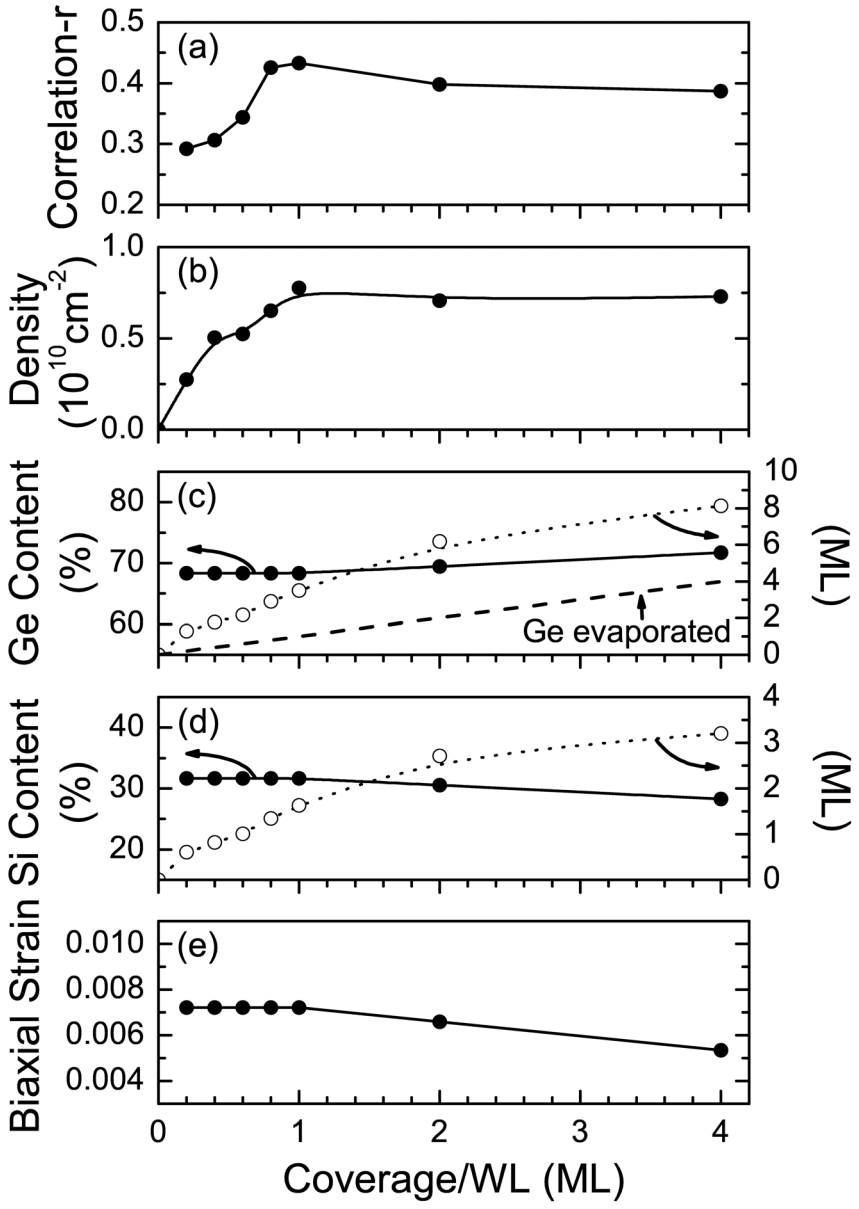

Figure 2.2: Evolution as a function of the coverage of: (a) the correlation coefficient r; (b) the island density; (c) the Ge content; (d) the Si content; and (e) the compressive biaxial strain (solid circles). Open circles in (c) and (d) show the total amounts of Ge and Si atoms in 3D islands calculated from the effective thickness on the wetting layer. The broken line in (c) shows the amount of deposited Ge atoms.

that trenches form around the islands indicating the transfer of the material to the growing islands [22]. As it is demonstrated below, this additional source of atoms plays an important role in the nucleation process.

In order to further understand the nucleation process, we evaluated the scaling behavior of the Voronoi cell areas and the grown 3D island volumes. The scaling function for the distribution of the Voronoi cell areas is described by the semiempirical gamma distribution (SGD) [8]:

$$\Pi_\alpha(x) = \frac{\alpha^\alpha}{\Gamma(\alpha)} x^{\alpha-1} \exp(-\alpha x) \tag{2.1}$$

where $\Gamma(\alpha)$ is Euler's gamma function and x is the Voronoi cell area scaled with its average value. The coefficient α denotes the degree of spatial correlation among nuclei and equals 3.61 for the Poissonian Voronoi network. Figure 2.3(a) shows the distribution of Voronoi cell areas fitted by the scaling function for each deposition amount. With increasing the surface coverage the scaled area distributions become narrower, thereby reflecting the increase of the coefficient α in Fig. 2.3(b). This implies the possibility for the kinetic self-ordering of 3D islands [23, 24]. Remarkably, this tendency continues even at the steady-state regime after deposition of 1.0 ML. The average area of the Voronoi cells then reaches about 1.4×10^4 nm^2 in accordance with the intuition that the half distance between 3D islands should be of the order of the diffusion length $\sim$ 70 nm on the wetting layer. Recently, Pimpinelli and Einstein showed that an excellent description of the capture zone size distribution can be obtained by the generalized Wigner distribution (GWD) [25]:

$$P_\beta(x) = a_\beta x^\beta \exp\left(-b_\beta x^2\right) \tag{2.2}$$

where the coefficient β is a parameter directly related to the critical nucleus size i with $\beta = i+1$. a_β and b_β are β-dependent constants determined by the normalization and the unit mean, respectively [26]. The nuclei that are composed of more than $i+1$ atoms grow to be further stable, but those with less than i atoms tend to decompose. The distribution of the scaled Voronoi cell area can be also fitted by the universal scaling function $P_\beta(x)$ [Fig. 2.3(a)]. The value of $\beta = 4.68$ yields the critical nucleus size $i \sim 4$ for the deposition of 1.0 ML where the Voronoi cells coincide with the

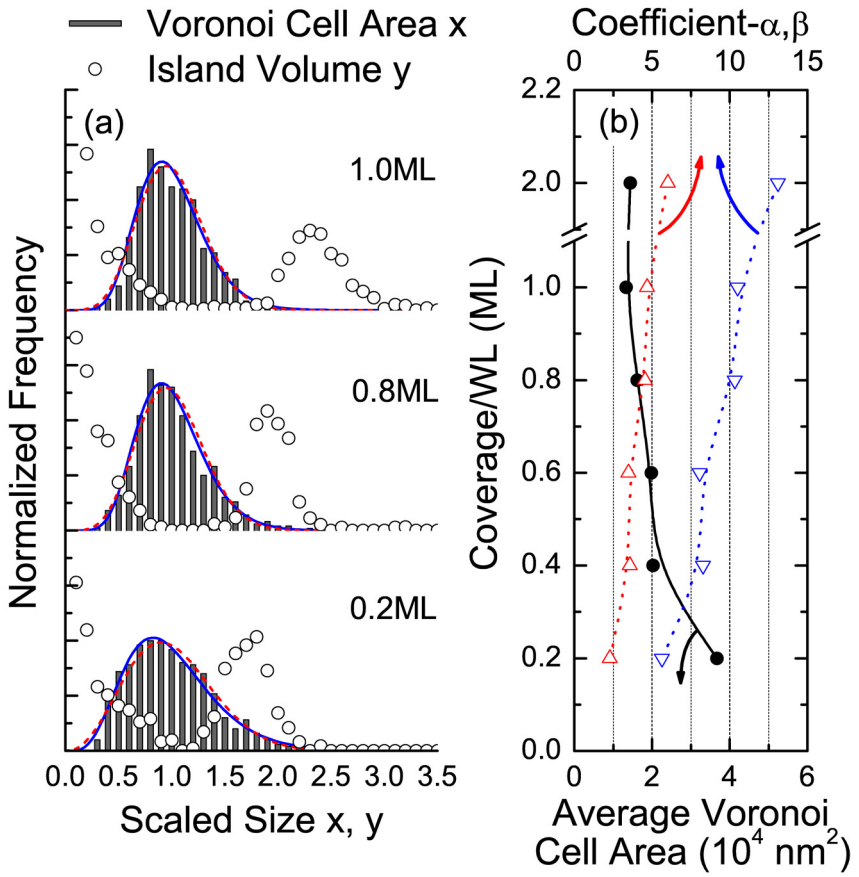

Figure 2.3: (a) Scaled distributions of Voronoi cell areas (vertical bars) fitted to two different scaling functions of the SGD (solid curves) and the GWD (short-broken curves), and scaled distributions of the experimental island size (open circles) in the submonolayer deposition range of 0.2, 0.8, and 1.0 ML on the wetting layer. x is the Voronoi cell area scaled with its average area, and y is the island volume scaled with its mean value. (b) Average area of the Voronoi cells (solid circles) and both coefficients of α (open downward triangles) and β (open upward triangles) as a function of Ge amount deposited on the wetting layer.

diffusion cells [Fig. 2.3(b)]. The obtained value of i may appear quite small when compared to the subcritical nucleus of several hundred atoms temporarily formed on the wetting layer at much lower temperature $T = 300$ °C [27]. In general, the higher growth temperature would require larger critical nuclei to trigger the nucleation since adatom detachment from a nucleus edge cannot be negligible. However, the mass transport from the SiGe alloy wetting layer in the present study is so significant that

not only Ge atoms but also Si atoms can be contained in the critical nucleus. The stronger bonding force of Si compared to that of Ge stabilizes the nucleus to reduce the critical nucleus size [28]. In the same line, the critical nucleus size of only $i = 9$ has been reported for the growth of Ge/Si(111) [29].

On the other hand, according to the capture zone model, also the distribution of the island volumes scaled with their mean volume is expected to follow a scaling function $f_i(y)$ such as the SGD and the GWD [25, 30]:

$$N_s(\Theta) = \frac{\Theta}{\langle s \rangle^2} f_i \left(\frac{s}{\langle s \rangle} \right) \tag{2.3}$$

where $N_s(\Theta)$ is the number of islands (normalized by the number of lattice sites) which is composed of s atoms and where $\langle s \rangle$ is the average number of atoms contained in islands. Here, $f_i(y)$ satisfies the sum rules $\int_0^\infty f_i(y)dy = \int_0^\infty f_i(y)ydy = 1$. This scale invariance also makes it possible to determine the critical nucleus size i. The statistical procedure was employed to describe the 2D homoepitaxial growth of Fe/Fe(001) [30, 31] and the 3D SK growth of InAs on GaAs(001) [10, 32–34]. In the latter case, the surface coverage of $\Theta = \sum sN_s$ is replaced by the effective thickness on the wetting layer, which is calculated from the total volume of 3D islands normalized to the area probed by AFM. Figure 2.3(a) shows the scaled distributions of the island size in the submonolayer deposition range of 0.2–1.0 ML on the 2D layer. Notice that none of the scaling functions above can represent the experimental data of bimodal distributions. The fact that the scaled size distributions have nonzero values around $y = 0$ resemble the characteristic observed in the distribution corresponding to the critical nucleus size $i = 0$ [30, 35]. The nucleus having the zero critical size implies that the nuclei can exist inherently as single adatom on the wetting layer surface. The defects present at the wetting layer surface mediate nucleation without critical size. For instance, step-edges and/or kinks are possible candidates for the nucleation sites. The growth of nucleus is encouraged by the substantial adatoms detached from the step-edges of wetting layer. Such anomalous scaling behaviors supported by the observation of the nucleation at the step-edges have been reported for the InAs islands on GaAs [10]. In particular, the bimodal distribution can be reproduced by the model accounting for both preferential nucleation sites and significant exchange processes

between deposited adatoms and the substrate atoms in the top surface [36]. This thermally activated exchange processes induce the incorporation of Si atoms into the nuclei at high temperature.

2.4 Raman Characterization of Composition and Strain

It is conceivable that the atomic interaction with the intermixed wetting layer occurs from the nucleation regime which can affect both the composition and strain in the growing islands. Here, Raman scattering spectroscopy was employed to probe the composition and strain states during the growth of Ge/Si nanoislands. Figure 2.4 shows Raman spectra obtained at different deposition amount of ^{76}Ge isotopes. The Raman spectrum of the wetting layer shows spectral features at $\sim$ 225, $\sim$ 302, and $\sim$ 435 cm^{-1} corresponding to 2TA(L), 2TA(X), and 2TA(Σ) phonons of the Si substrate, respectively. No clear Raman feature due to the 4.4 ML 2D layer has appeared in accordance with the previous reports [37, 38]. Three peaks are observed at $\sim$290, $\sim$408, and $\sim$520 cm^{-1}, which are assigned to ^{76}Ge-^{76}Ge, Si-^{76}Ge, and Si-Si modes respectively. As the nucleation and island growth proceeds on the wetting layer, the Raman signals of the ^{76}Ge-^{76}Ge and Si-^{76}Ge modes become more pronounced. Note that the ^{76}Ge-^{76}Ge peak is separately observed on the lower-frequency shoulder of the substrate 2TA(X) peak due to the isotope effect [39]. The Ge-Ge mode arising from Ge having natural isotopic abundance would have overlapped completely with the substrate 2TA(X) peak. Hence, the use of enriched ^{76}Ge isotope source enables us to probe the faint signals of the small-sized 3D islands formed by submonolayer deposition. Figures 2.2(c)-2.2(e) show the average SiGe composition and compressive biaxial strain inside 3D islands that are determined from the peak positions of the ^{76}Ge-^{76}Ge and Si-^{76}Ge modes [16]. $b_{\text{Ge-Ge}} = -400$ cm^{-1} and $b_{\text{Si-Ge}} = -575$ cm^{-1} are used as the strain-shift coefficients [37], and the isotopic shift due to ^{76}Ge is taken into account. Figures 2.2(c) and 2.2(d) also display the absolute amounts of Si and Ge atoms in the 3D islands estimated from the effective thickness on the wetting layer. Remarkably, the amounts of both Si and Ge atoms incorporated into 3D islands sur-

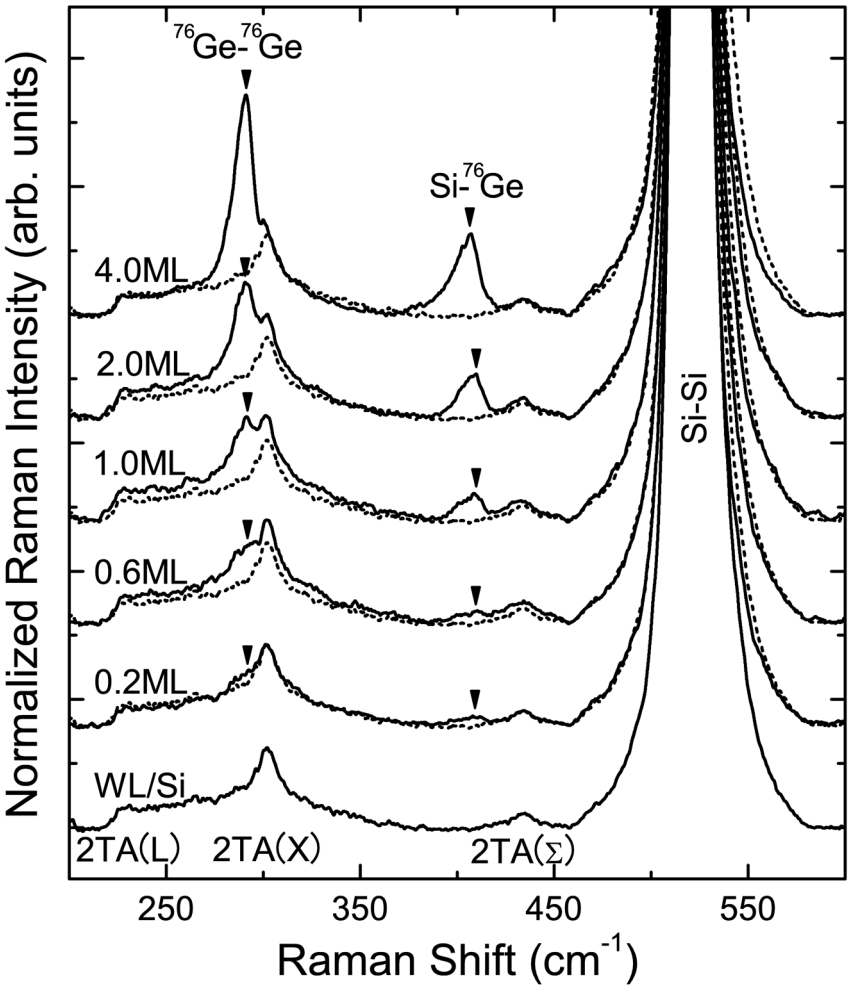

Figure 2.4: Raman spectra obtained for different ^{76}Ge deposition amounts on the wetting layer. All spectra are normalized to the Si-Si mode of the substrate. For comparison, Raman spectrum of the wetting layer having the critical thickness (the bottom spectrum) is overlapped as the dotted curves with each spectrum.

pass the number of the evaporated Ge atoms on the wetting layer for the deposition of 0.2 ML, indicating that most of the atoms in nuclei are supplied from the SiGe alloy wetting layer at the nucleation regime. This implies that the initial strained SiGe alloy wetting layer is largely decomposed and incorporated into the more relaxed 3D islands when the deposition reaches 2.0 ML. Such a strong interaction with the metastable 2D layer has been observed also during formation of hut clusters at

relatively low temperature [40]. Above 2.0 ML, the incorporation rate of Ge atoms approaches asymptotically the Ge deposition rate. This suggests that most of Ge adatoms deposited within the diffusion cells contribute to the growth of 3D islands. In parallel, Si atoms are further incorporated from the exposed silicon substrate.

The compressive strain inside the 3D islands relaxes as a general trend beyond the deposition amount of 1.0 ML [Fig. 2.2(e)]. It is well-known that a large fraction of pyramids appears to undergo the pyramid-to-dome shape transition as a path for the partial relaxation of strain while some of the relatively strained pyramids decay [14]. Note that the pyramid-derived plots in Fig. 2.1 progressively approach zero. The atoms released from the decaying pyramids contribute to the further growth of the adjacent relaxed domes as observed in the growth of InAs on GaAs(001) [41]. The driving force for the island-island interaction is known to be the strain fields present around 3D islands [23]. When the 3D islands get close to each other, the interference of the strain fields induces a biased surface diffusion [42]. Hence, the newly deposited Ge adatoms are not necessarily incorporated into the nearest neighboring islands. The effective capture zones around strained pyramids shrink whereas those around the neighboring relaxed domes expand. Therefore the simple capture zone model assuming a correlation coefficient of unity does not hold at the steady-state regime [Fig. 2.2(a)]. Furthermore, the coefficient α maintains a steady increase all the way up to the deposition of 2.0 ML [Fig. 2.3(b)] while the correlation coefficient r decreases after 1.0 ML [Figs. 2.2(a)]. The continuous lateral ordering can occur in conjunction with the strain-driven repulsive motions of closely spaced 3D islands [43, 44].

2.5 Conclusions

The nucleation and growth of Ge/Si(001) SK nanoisland have been investigated at temperature of $T = 620$ °C. The correlation between the grown island volumes and the corresponding Voronoi cell areas shows clearly that the growth of the 3D islands does not follow the simple capture zone model. In addition to the deposited Ge adatoms, the material transferred from the alloyed 2D layer and underlying substrate contributes also to the growth of the strained islands. The atomic number of critical

nucleus size is obtained from the scaling analysis of the distribution of the Voronoi cell areas. The experimental values of i, much smaller than anticipated, suggest that the simultaneous incorporation of Si atoms have a thermally stabilizing effect on the nuclei. The strong interaction with the metastable 2D layer was found to occur from the nucleation regime. This is supported by the composition within the islands formed at the early stage of the growth process, which was determined from Raman analysis combined with ^{76}Ge isotope tracing. As soon as the 2D layer reaches the critical thickness, the formation of the nuclei is accelerated by the erosion of the intermixed 2D layer. When the surface is fully covered by the diffusion cells at the steady-state regime, most of the adatoms contribute to the growth of the existing 3D islands and no more nucleation takes place. The decrease of the distance between the neighboring islands promotes the strain-driven atomic transport especially between the strained pyramids and the adjacent relaxed domes. At the same time, the deposited Ge adatoms are not necessarily incorporated into the nearest neighboring islands. The island-island interaction unevenly deforms the capture zones around the islands of different sizes, leading to further lateral ordering.

References

[1] J. Stangl, V. Holý, and G. Bauer, Rev. Mod. Phys. **76**, 725 (2004).

[2] I. N. Stranski and L. Krastanow, Sitzungsber. Akad. Wiss. Wien, Math.-Naturwiss. Kl., Abt. 2B **146**, 797 (1938).

[3] M. Kästner and B. Voigtländer, Phys. Rev. Lett. **82**, 2745 (1999).

[4] R. E. Rudd, G. A. D. Briggs, A. P. Sutton, G. Medeiros-Ribeiro, and R. S. Williams, Phys. Rev. Lett. **90**, 146101 (2003).

[5] K. Shibata and K. Hirakawa, Appl. Phys. Lett. **93**, 062101 (2008); M. Jung, T. Machida, K. Hirakawa, S. Komiyama, T. Nakaoka, S. Ishida, and Y. Arakawa, *ibid.* **87**, 203109 (2005).

[6] K. Nakajima, A. Konishi, and K. Kimura, Phys. Rev. Lett. **83**, 1802 (1999).

[7] X. R. Qin, B. S. Swartzentruber, and M. G. Lagally, Phys. Rev. Lett. **84**, 4645 (2000).

[8] P. A. Mulheran and J. A. Blackman, Phys. Rev. B **53**, 10261 (1996).

[9] F. Ratto, A. Locatelli, S. Fontana, S. Kharrazi, S. Ashtaputre, S. K. Kulkarni, S. Heun, and F. Rosei, Phys. Rev. Lett. **96**, 096103 (2006); F. Ratto, Ph.D. thesis, Universite du Quebec, 2007.

[10] M. Fanfoni, E. Placidi, F. Arciprete, E. Orsini, F. Patella, and A. Balzarotti, Phys. Rev. B **75**, 245312 (2007); F. Arciprete, E. Placidi, V. Sessi, M. Fanfoni, F. Patella, and A. Balzarotti, Appl. Phys. Lett. **89**, 041904 (2006); E. Placidi, F. Arciprete, V. Sessi, M. Fanfoni, F. Patella, and A. Balzarotti, *ibid.* **86**, 241913 (2005).

[11] B. Voigtländer, Surf. Sci. Rep. **43**, 127 (2001).

[12] G. Katsaros, G. Costantini, M. Stoffel, R. Esteban, A. M. Bittner, A. Rastelli, U. Denker, O. G. Schmidt, and K. Kern, Phys. Rev. B **72**, 195320 (2005).

[13] T. U. Schülli, M.-I. Richard, G. Renaud, V. Favre-Nicolin, E. Wintersberger, and G. Bauer, Appl. Phys. Lett. **89**, 143114 (2006).

[14] F. M. Ross, J. Tersoff, and R. M. Tromp, Phys. Rev. Lett. **80**, 984 (1998).

[15] A. Rastelli, M. Stoffel, J. Tersoff, G. S. Kar, and O. G. Schmidt, Phys. Rev. Lett. **95**, 026103 (2005).

[16] M. I. Alonso, M. de la Calle, J. O. Ossó, M. Garriga, and A. R. Goñi, J. Appl. Phys. **98**, 033530 (2005).

[17] A. V. Baranov, A. V. Fedorov, T. S. Perova, R. A. Moore, V. Yam, D. Bouchier, V. Le Thanh, and K. Berwick, Phys. Rev. B **73**, 075322 (2006).

[18] A. Malachias, S. Kycia, G. Medeiros-Ribeiro, R. Magalhães-Paniago, T. I. Kamins, and R. S. Williams, Phys. Rev. Lett. **91**, 176101 (2003).

[19] T. U. Schülli, M. Stoffel, A. Hesse, J. Stangl, R. T. Lechner, E. Wintersberger, M. Sztucki, T. H. Metzger, O. G. Schmidt, and G. Bauer, Phys. Rev. B **71**, 035326 (2005).

[20] A. Ishizaka and Y. Shiraki, J. Electrochem. Soc. **133**, 666 (1986).

[21] M. Li, M. C. Bartelt, and J. W. Evans, Phys. Rev. B **68**, 121401(R) (2003).

[22] U. Denker, O. G. Schmidt, N. Y. Jin-Philipp, and K. Eberl, Appl. Phys. Lett. **78**, 3723 (2001).

[23] M. Meixner, E. Schöll, V. A. Shchukin, and D. Bimberg, Phys. Rev. Lett. **87**, 236101 (2001); M. Meixner, E. Schöll, M. Schmidbauer, H. Raidt, and R. Köhler, Phys. Rev. B **64**, 245307 (2001).

[24] B. Cho, T. Schwarz-Selinger, K. Ohmori, D. G. Cahill, and J. E. Greene, Phys. Rev. B **66**, 195407 (2002).

[25] A. Pimpinelli and T. L. Einstein, Phys. Rev. Lett. **99**, 226102 (2007); B. R. Conrad, E. Gomar-Nadal, W. G. Cullen, A. Pimpinelli, T. L. Einstein, and E. D. Williams, Phys. Rev. B **77**, 205328 (2008).

[26] $a_\beta = 2\Gamma\left(\frac{\beta+2}{2}\right)^{\beta+1}/\Gamma\left(\frac{\beta+1}{2}\right)^{\beta+2}$ and $b_\beta = \left[\Gamma\left(\frac{\beta+2}{2}\right)/\Gamma\left(\frac{\beta+1}{2}\right)\right]^2$.

[27] D. E. Jesson, M. Kästner, and B. Voigtländer, Phys. Rev. Lett. **84**, 330 (2000).

[28] V. Cherepanov and B. Voigtländer, Phys. Rev. B **69**, 125331 (2004).

[29] A. A. Shklyaev, M. Shibata, and M. Ichikawa, Surf. Sci. **416**, 192 (1998).

[30] J. G. Amar and F. Family, Phys. Rev. Lett. **74**, 2066 (1995).

[31] J. A. Stroscio and D. T. Pierce, Phys. Rev. B **49**, 8522(R) (1994).

[32] V. Bressler-Hill, S. Varma, A. Lorke, B. Z. Nosho, P. M. Petroff, and W. H. Weinberg, Phys. Rev. Lett. **74**, 3209 (1995).

[33] Y. Ebiko, S. Muto, D. Suzuki, S. Itoh, K. Shiramine, T. Haga, Y. Nakata, and N. Yokoyama, Phys. Rev. Lett. **80**, 2650 (1998).

[34] T. J. Krzyzewski, P. B. Joyce, G. R. Bell, and T. S. Jones, Phys. Rev. B **66**, 201302(R) (2002).

[35] D. D. Chambliss and K. E. Johnson, Phys. Rev. B **50**, 5012(R) (1994).

[36] R. Miranda and J. M. Gallego, Phys. Rev. B **64**, 085426 (2001).

[37] P. H. Tan, K. Brunner, D. Bougeard, and G. Abstreiter, Phys. Rev. B **68**, 125302 (2003).

[38] O. Moutanabbir, S. Miyamoto, A. Fujimoto, and K. M. Itoh, J. Cryst. Growth **301-302**, 324 (2007).

[39] A. V. Kolobov, K. Morita, K. M. Itoh, and E. E. Haller, Appl. Phys. Lett. **81**, 3855 (2002).

[40] M. Horn-von Hoegen, B. H. Müller, T. Grabosch, and P. Kury, Phys. Rev. B **70**, 235313 (2004).

[41] T. R. Ramachandran, R. Heitz, P. Chen, and A. Madhukar, Appl. Phys. Lett. **70**, 640 (1997).

[42] M. Stoffel, A. Rastelli, S. Kiravittaya, and O. G. Schmidt, Phys. Rev. B **72**, 205411 (2005).

[43] U. Denker, A. Rastelli, M. Stoffel, J. Tersoff, G. Katsaros, G. Costantini, K. Kern, N. Y. Jin-Phillipp, D. E. Jesson, and O. G. Schmidt, Phys. Rev. Lett. **94**, 216103 (2005).

[44] G. Capellini, M. De Seta, F. Evangelisti, V. A. Zinovyev, G. Vastola, F. Montalenti, and Leo Miglio, Phys. Rev. Lett. **96**, 106102 (2006).

Chapter III

Excitonic Aharonov-Bohm Effect in Ge/Si Type-II Quantum Dots

We report on a magneto-photoluminescence study of isotopically pure ^{70}Ge/Si self-assembled type-II quantum dots. Oscillatory behaviors attributed to the Aharonov-Bohm effect are simultaneously observed for the emission energy and intensity of excitons subject to an increasing magnetic field. When the magnetic flux penetrates through the ring-like trajectory of an electron moving around each quantum dot, the ground state of an exciton experiences a change in its angular momentum. Our results provide the experimental evidence for the phase coherence of a localized electron wave function in Ge/Si self-assembled quantum structures.

This Chapter has been submitted to Physical Review Letters.

3.1 Introduction

The wave function of a charged particle circulating around a magnetic field region acquires a phase shift proportional to the magnetic flux threading the closed path. This topological quantum effect, well known as the Aharonov-Bohm (AB) effect [1], manifests as quantum interference of the particle wave function with the period of the universal flux quantum $\Phi_0 = hc/e$. Tonomura *et al.* provided the first conclusive experimental evidence for the existence of the AB effect by using magnetic fields shielded from an electron wave [2]. Recent advances in lithography and growth techniques make it possible to observe the AB effect in the magneto-transport properties of semiconductor quantum rings within the experimentally available range of magnetic fields [3, 4]. In addition to this electronic AB effect, the possibility of the AB effect to occur for an exciton placed in a magnetic field was predicted assuming that the electron and hole move around with different ring-like trajectories [5–8]. Such an excitonic variety of the AB effect has been exclusively reported for compound semiconductor quantum structures such as InGaAs/GaAs patterned quantum rings [9], InAs/InP quantum tubes [10], InP/GaAs and ZnTe/ZnSe self-assembled type-II quantum dots (QDs) [11–15]. In particular, the type-II QD enhances internal polarization of neutral exciton since the electron and hole are spatially separated. The radial dipole moment accumulates the AB phase mainly during the coherent motion of either electron or hole that rotates around the QD in the presence of perpendicular magnetic fields. This leads to a strong AB effect in the magneto-optical properties of such QD systems.

In spite of being fundamentally and technologically highly relevant, AB studies of Si-based quantum systems are conspicuously missing in the literature. It is known that Ge quantum-size hut clusters embedded in a Si matrix are classified as type-II QDs [16, 17]. The photoluminescence (PL) emission from these structures has been subject of intensive investigations as it offers a wealth of information on their structural and optical properties [18]. To the best of our knowledge, however, the PL studies on the Ge/Si self-assembled type-II QDs have never reported the excitonic

AB effects. In this Chapter, we report the first observation of the AB effect on the bound excitons around the Ge/Si QDs. The magneto-PL measurements show clear oscillations of the emission energy and intensity against the magnetic fields providing clear experimental evidence of phase coherence of the electron wave function localized at the tensile-strained Si layer surrounding Ge QD.

3.2 Experimental Details

A Ge/Si hut cluster superlattice was grown via the Stranski-Krastanov growth mode by solid-source molecular beam epitaxy (MBE). A p-type FZ-Si(001) substrate was chemically cleaned using the Ishizaka-Shiraki method [19] before being introduced into the MBE chamber. The protective oxide film was desorbed in an ultra high vacuum by annealing the substrate at 800 °C. The thermal treatment was followed by 6-ML Ge deposition at the growth temperature of 540 °C. In order to avoid the random magnetic fluctuations arising from the ^{73}Ge isotopes, which have non-zero nuclear spins, an isotopically purified solid source of ^{70}Ge possessing zero nuclear spin was used. The low-temperature epitaxial growth resulted in the kinetic formation of defect-free hut clusters with both relatively small size distribution and high density in the order of 10^{11} cm^{-2}. Figure 3.1(a) displays an image of typical morphology observed by *ex-situ* atomic force microscope (AFM) in tapping mode. The dimensions of the uncapped hut clusters were 31.8 ± 4.5 nm in length and width, and 1.3 ± 0.3 nm in height. Immediately after the Ge deposition, the hut cluster layer was covered with a 15 nm-thick undoped Si spacer in order to reduce the vertical correlation which gives an additional factor for size dispersion [20]. This stacking sequence was repeated to grow a 20-period QD superlattice that was free of visible dislocations [Fig. 3.1(b)]. Residual defects unintentionally incorporated during the low-temperature growth [21] were predominantly annihilated by 1 s rapid thermal annealing (RTA) at 730 °C in an argon ambient [22]. The post-annealed sample was mounted in a strain-free manner and immersed in a superfluid liquid helium bath at the temperature of $T = 2$ K. Low-temperature PL measurements were carried out by applying a

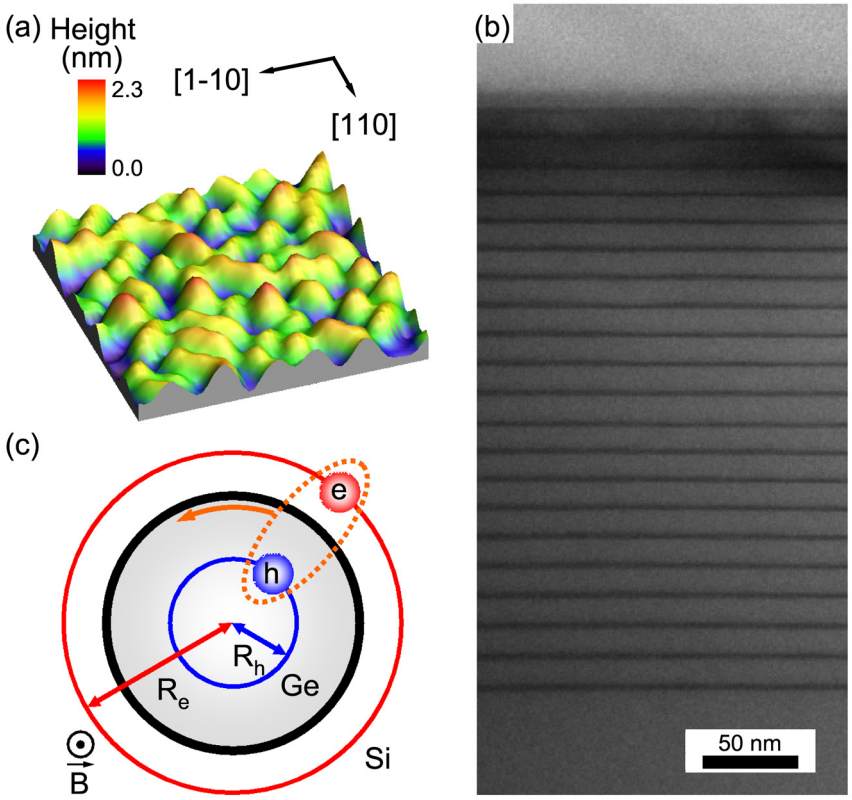

Figure 3.1: (a) AFM image of the Ge/Si hut clusters formed by 6-ML Ge deposition at 540 °C (200 × 200 nm^2). (b) Cross-sectional transmission electron microscope image of an as-grown superlattice comprising 20 periods of hut cluster layers separated by 15-nm Si layers. (c) Schematic illustration of the spatial configuration of electron and hole in the Ge/Si type-II QD.

magnetic field B up to 5 T in the Faraday configuration. The 514.5 nm line of an Ar^+ laser was employed as an excitation source. The photogenerated holes are tightly trapped by the Ge QDs while the electrons are weakly bound and extended into the Si regions [Fig. 3.1(c)]. In addition to the Coulomb attraction, a built-in tensile strain in Si also creates an attractive potential for the electrons around QDs [16]. The luminescence emission from the QDs were guided to a Bomem DA 8 Fourier transform interferometer having a spectral resolution of 250 μeV, and detected by a liquid nitrogen-cooled InSb photodetector.

3.3 Excitation Power Dependence

Figure 3.2(a) shows the zero-field PL spectra recorded with varying excitation powers. The intense luminescence arises from the phononless radiative recombination [16]. The spectra extend to energies below the band gap of the unstrained bulk Ge supporting the observation that the grown hut clusters have the type-II band alignment [17]. We observe no clear PL features related to dislocations [23] and impurities which can lead to a modification in the excitonic AB oscillations [12, 24]. Remarkably, the integrated PL intensity displays a sublinear power dependency on the excitation power above 7 mW/cm^2 [Fig. 3.2(b)]. The asymptotical power exponent of $m \sim 0.67$ has been predicted when Auger recombination process exists as a competitive nonradia-

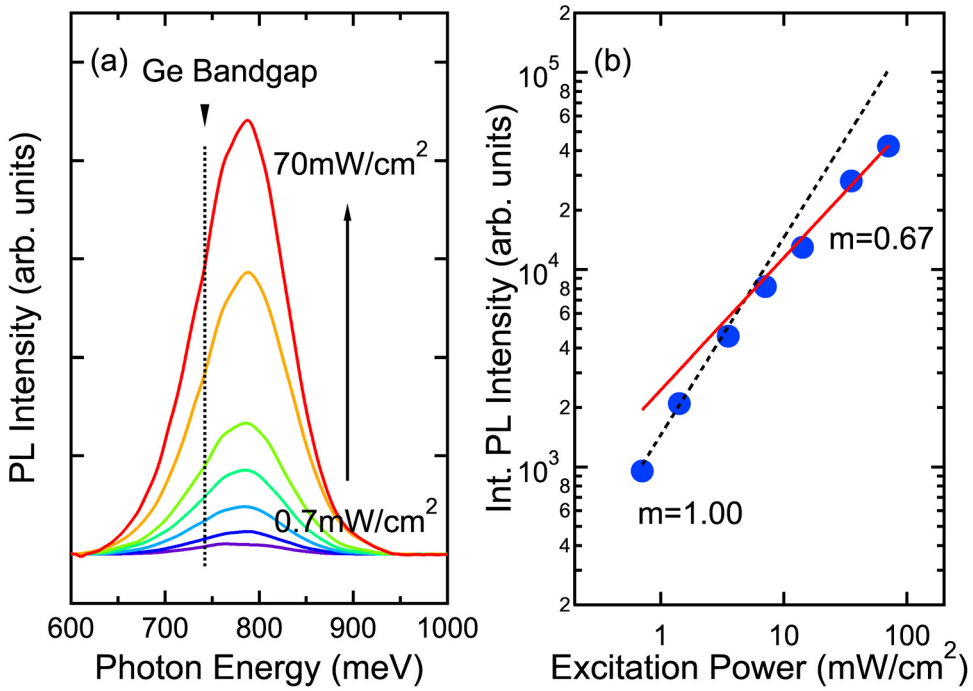

Figure 3.2: (a) Zero-field PL spectra measured with the excitation power between 0.7 and 70 mW/cm^2. The vertical dashed line indicates the bandgap position of the unstrained bulk Ge at $T = 2$ K. (b) Power dependence $I_{\mathrm{PL}} \propto P_{\mathrm{exc}}^{m}$ of the intensity obtained by integration of the PL spectra. The power exponent asymptotically changes from $m = 1.00$ (dotted line) to $m = 0.67$ (solid line).

tive channel [25]. In such cases, the PL energy is expected to show a blue shift due to the many-body effects [26]. The present experimental results show the same phenomena as observed for PL properties of the type-II Ge/Si hut clusters with high excitation powers [16]. Meanwhile, a linearly dependent regime can be observed at weaker excitation power, which is difficult to be achieved in the single-layer structure aforementioned. This is possibly attributed to the experimental fact that the Auger recombination process is sufficiently suppressed owing to the use of the multi-layer structure [27]. The excitation power density of 3.5 mW/cm^2 used for the observation of the excitonic AB oscillations populates less than one exciton per QD. During a relatively long recombination time caused by a large wave-function separation [26], those single excitons almost relax to the ground states. Thereafter the PL measurements of the Ge/Si type-II QDs can assign the ground-state spectrum of the single excitons.

3.4 Magneto-Photoluminescence Properties

Figure 3.3 shows the PL spectra of Ge/Si hut cluster superlattice recorded at two different magnetic fields, $B = 0.8$ T and $B = 1.8$ T. The PL intensity is reduced with increasing magnetic field. The spectra are fitted well with single Gaussian curves, from which the peak positions are determined. The application of the magnetic fields induces an overall peak shift in the order of a few meV. Figures 3.4(b)-(d) show the detailed evolution of the PL intensity and the peak energy as a function of the magnetic field. Oscillatory behaviors are observed for both energy and intensity providing a clear signature of the excitonic AB effect.

The origin of the oscillation of the peak energy can be explained as follows. The energy of the single exciton with a definite angular momentum (projection), L, is described by [8]:

$$E_{exc}(B) = E_g + \frac{\hbar^2}{2MR_0^2}\left(L + \frac{\Delta\Phi}{\Phi_0}\right)^2 \tag{3.1}$$

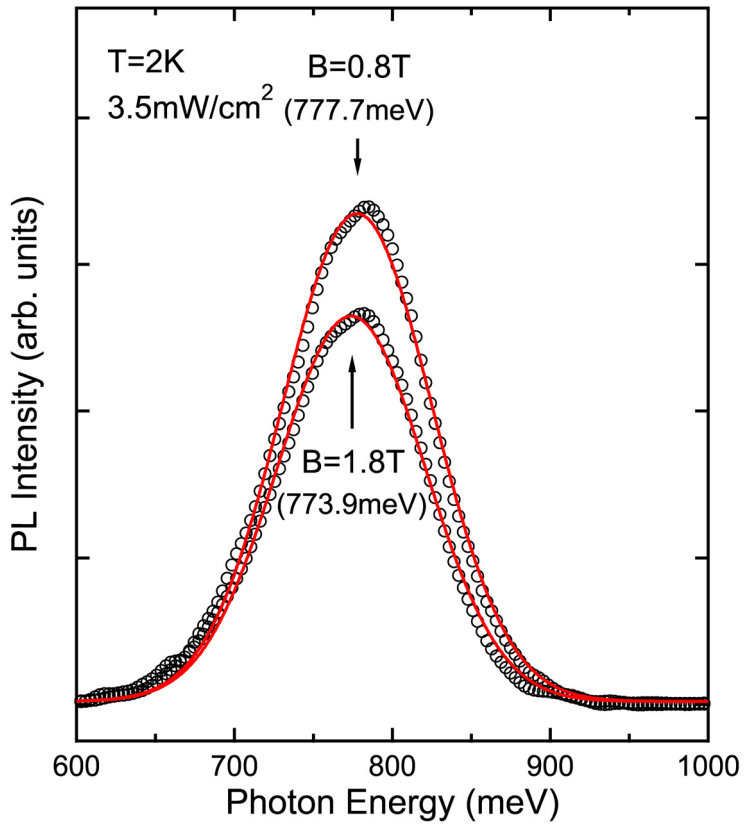

Figure 3.3: PL spectra of the Ge/Si hut cluster superlattice recorded at 2 K for the two magnetic fields, $B = 0.8$ T and $B = 1.8$ T. In order to extract the peak positions, the experimental data are fitted with single Gaussian curves (solid lines). The arrows indicate the fitted peak energy.

where E_g is the energy gap including the exciton binding energy. $M = (m_e R_e^2 + m_h R_h^2)/R_0^2$ and $R_0 = (R_e + R_h)/2$ are here defined for describing the rotation Hamiltonian of the whole exciton along the ring-like trajectory (see Fig. 3.1(c)), where $m_{e(h)}$ and $R_{e(h)}$ are the effective mass and orbital radius of the electron (hole), respectively. Assuming that the hole is localized strongly within the QD, i.e. $R_h \approx 0$, the magnetic flux threading the region between the electron and hole orbital rings is given by $\Delta\Phi = \pi R_e^2 B$. As illustrated in Fig. 3.4(a), the second term in Eq. (3.1) shows the quadratic dependence of the excitonic energy on the magnetic field for different values of L. At zero magnetic field, the ground state of the exciton takes a

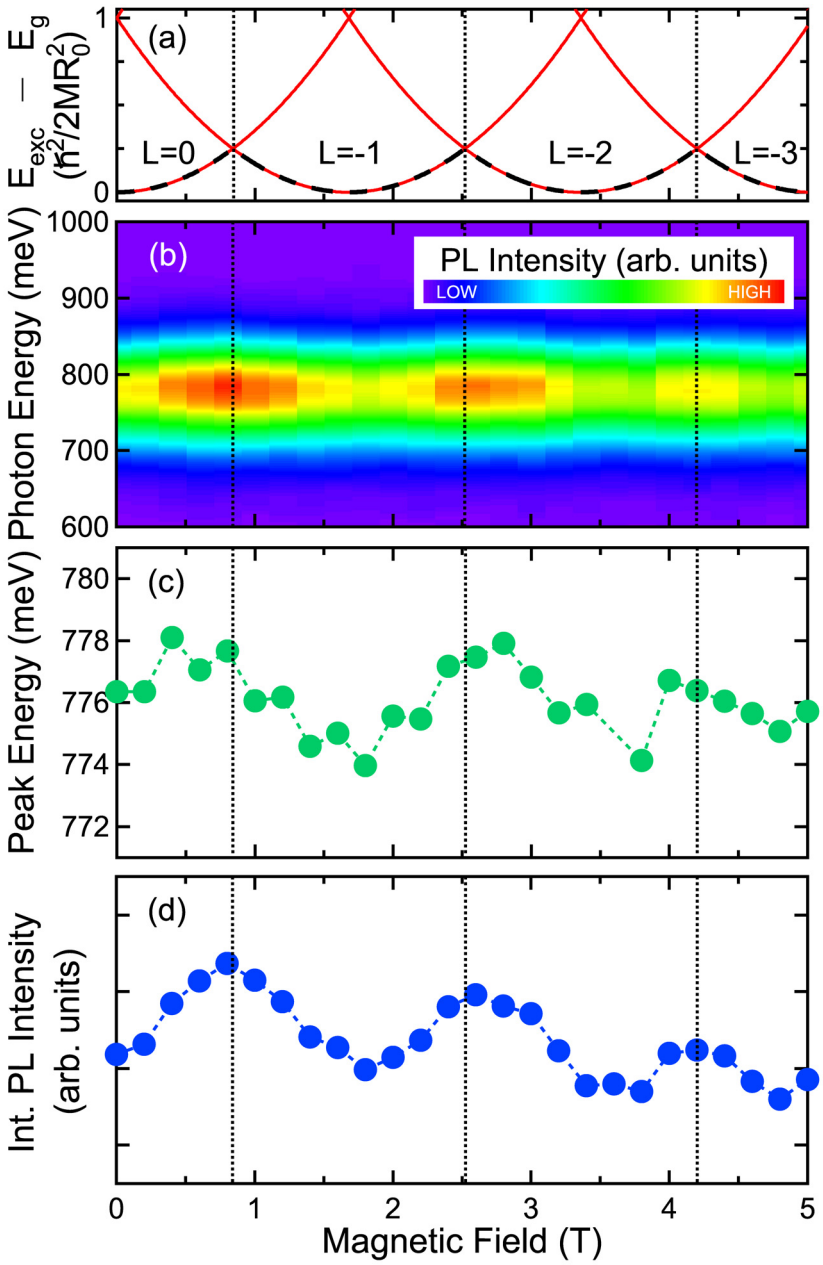

Figure 3.4: (a) Magnetic-field dependence of the quadratic contribution in Eq. (3.1) representing the excitonic energy for an angular momentum L. The dashed line marks the energetic transition for ground-state exctions. (b) Contour plot of the PL spectra as a function of the magnetic fields. Detailed evolutions of (c) the peak energy and (d) the integrated PL intensity. The vertical dotted lines indicate the magnetic fields at which the angular momentum transition takes place. The magnetic-field separation between the neighboring dotted lines corresponds to the flux quantum Φ_0.

zero angular momentum $L = 0$. With increasing magnetic field, the angular momentum makes a series of ground-state transition to $L = -1$, -2, and -3 for the half integer flux quanta. Then the energy of the ground-state exciton oscillates with the magnetic-field period of $\Phi_0/\pi R_e^2$ along the dashed line in Fig. 3.4(a). This qualitative account is in good agreement with the oscillation of the peak energy observed in Fig. 3.4(c). We believe that a certain level of damping is due to inhomogeneity associated with the QD ensembles similarly to the previous observation in InP/GaAs system [11]. It should be noted that the absolute value of the angular momentum $|L|$ denotes the number of threading flux quanta. In Fig. 3.4(c), the oscillation is sustained up to magnetic fields corresponding to three flux quanta. From the period of AB oscillations, the average radius of coherent electron motion is estimated to be $R_e \sim 28$ nm. This orbital diameter, $2R_e$, is slightly larger than the structural size measured by AFM although unavoidable intermixing during the growth and RTA may modify the Si-Ge interface. These observations provide the experimental evidence that an electron localized in Si outside the Ge QD maintains phase coherence long enough to demonstrate the AB effect.

Figure 3.4(d) shows an oscillatory behavior of the PL intensity that is in phase with the oscillation of the peak energy. However, the simplified picture of the electron travelling with the constant orbital radius of R_e cannot explain the oscillation of the PL intensity. As a matter of fact, increasing the magnetic field tends to push the electron wave function closer to the QD boundary [7]. A complication is the assumption that the diameter is constant in Eq. (3.1) breaks down as soon as we introduce the concept of variable diameter. In case of a decrease in the diameter, it can enlarge the overlap of the electron and hole wave functions, thereby resulting in the monotonic enhancement of the PL intensity. On the other hand, the angular momentum transition from L to $L - 1$ should accompany the expansion of the electron trajectory [7] and suppress the PL intensity abruptly. Hence the interplay between localization and delocalization of electrons periodically switches the PL intensity. However, the intensity oscillation shown in Fig. 3.4(d) does not necessarily represent a saw-tooth shape but a sinusoidal one, which can be attributed to the fact that the excitonic populations are thermally distributed in the ground states

as well as the excited states at finite temperature [Fig. 3.4(a)]. In principle, the selection rule that the optically bright transitions are allowed only for the excitons with $L = 0$ is valid in the nanostructures with a perfect rotational symmetry. Due to the asymmetric shape of typical hut clusters elongated in [100] directions (see Fig. 3.1(a)), the partial relaxation of the selection rules can activate the dark excitons with $L \neq 0$ [12,24]. The amplitude of the PL intensity oscillation thus decreases as a general trend but persists even after each angular momentum transition.

3.5 Conclusions

In conclusion, we have presented the AB signature of the ground-state excitonic energy through magneto-PL measurements on isotopically pure ^{70}Ge/Si self-assembled type-II QDs. The localized electrons in the tensile-strained Si surrounding region display sufficient coherence to exhibit the AB effect, which allows us to observe the penetration of flux quanta (up to three) through the trajectory of the electron circulating around QD. Oscillatory behavior of the PL intensity in phase with that of the excitonic energy was also demonstrated. Such synchronized oscillations cannot be understood in the framework of a simplified theory assuming the constant diameter of electron motion around the QD. Although further investigations are necessary to comprehend the oscillatory behaviors of both the emission energy and intensity observed above, these oscillations suggest the possibility to tailor the optical properties of Si-based nanostructures by a controlled application of magnetic fields.

References

[1] Y. Aharonov and D. Bohm, Phys. Rev. **115**, 485 (1959).

[2] A. Tonomura, N. Osakabe, T. Matsuda, T. Kawasaki, J. Endo, S. Yano, and H. Yamada, Phys. Rev. Lett. **56**, 792 (1986).

[3] W. X. Gao, K. Ismail, K. Y. Lee, J. O. Chu, and S. Washburn, Appl. Phys. Lett. **65**, 3114 (1994).

[4] A. Fuhrer, S. Lüscher, T. Ihn, T. Heinzel, K. Ensslin, W. Wegscheider, and M. Bichler, Nature (London) **413**, 822 (2001).

[5] A. V. Chaplik, JETP Lett. **62**, 900 (1995).

[6] A. B. Kalameitsev, V. M. Kovalev, and A. O. Govorov, JETP Lett. **68**, 669 (1998).

[7] K. L. Janssens, B. Partoens, and F. M. Peeters, Phys. Rev. B **64**, 155324 (2001).

[8] A. O. Govorov, S. E. Ulloa, K. Karrai, and R. J. Warburton, Phys. Rev. B **66**, 081309(R) (2002).

[9] M. Bayer, M. Korkusinski, P. Hawrylak, T. Gutbrod, M. Michel, and A. Forchel, Phys. Rev. Lett. **90**, 186801 (2003).

[10] K. Tsumura, S. Nomura, P. Mohan, J. Motohisa, and T. Fukui, Jpn. J. Appl. Phys. **46**, L440 (2007).

[11] E. Ribeiro, A. O. Govorov, W. Carvalho, Jr., and G. Medeiros-Ribeiro, Phys. Rev. Lett. **92**, 126402 (2004).

[12] M. H. Degani, M. Z. Maialle, G. Medeiros-Ribeiro, and E. Ribeiro, Phys. Rev. B **78**, 075322 (2008).

[13] I. L. Kuskovsky, W. MacDonald, A. O. Govorov, L. Mourokh, X. Wei, M. C. Tamargo, M. Tadic, and F. M. Peeters, Phys. Rev. B **76**, 035342 (2007).

[14] I. R. Sellers, V. R. Whiteside, I. L. Kuskovsky, A. O. Govorov, and B. D. McCombe, Phys. Rev. Lett. **100**, 136405 (2008).

[15] I. R. Sellers, V. R. Whiteside, A. O. Govorov, W. C. Fan, W-C. Chou, I. Khan, A. Petrou, and B. D. McCombe, Phys. Rev. B **77**, 241302(R) (2008).

[16] M. W. Dashiell, U. Denker, and O. G. Schmidt, Appl. Phys. Lett. **79**, 2261 (2001).

[17] U. Denker, M. Stoffel, O. G. Schmidt, and H. Sigg, Appl. Phys. Lett. **82**, 454 (2003).

[18] see for e.g. M. W. Dashiell, U. Denker, C. Müller, G. Costantini, C. Manzano, K. Kern, and O. G. Schmidt, Appl. Phys. Lett. **80**, 1279 (2002).

[19] A. Ishizaka and Y. Shiraki, J. Electrochem. Soc. **133**, 666 (1986).

[20] O. G. Schmidt, U. Denker, S. Christiansen, and F. Ernst, Appl. Phys. Lett. **81**, 2614 (2002).

[21] N. Usami, S. Fukatsu, and Y. Shiraki, Appl. Phys. Lett. **61**, 1706 (1992).

[22] O. Moutanabbir, S. Miyamoto, A. Sagara, H. Oshikawa, and K. M. Itoh, Thin Solid Films **517**, 391 (2008).

[23] N. Usami, F. Issiki, D. K. Nayak, Y. Shiraki, and S. Fukatsu, Appl. Phys. Lett. **67**, 524 (1995).

[24] L. G. G. V. Dias da Silva, S. E. Ulloa, and A. O. Govorov, Phys. Rev. B **70**, 155318 (2004).

[25] P. Apetz, L. Vescan, A. Hartmann, C. Dieker, and H. Lüth, Appl. Phys. Lett. **66**, 445 (1995).

[26] B. V. Kamenev, E.-K. Lee, H.-Y. Chang, H. Han, H. Grebel, L. Tsybeskov, and T. I. Kamins, Appl. Phys. Lett. **89**, 153106 (2006).

[27] T. Tayagaki, S. Fukatsu, and Y. Kanemitsu, Phys. Rev. B **79**, 041301(R) (2009).

Chapter IV

Escape Dynamics of a Few Electrons in Single-Electron Ratchet

Transport dynamics of a few electrons in a quantum dot are investigated in a single-electron ratchet using silicon nanowire metal-oxide-semiconductor field-effect transistors. Time-resolved measurements in a nanosecond regime are carried out to determine the escape times of the first, second, and third electrons from the quantum dot originally containing three electrons. The escape time strongly depends on the number of electrons due to the single-electron charging effect in the quantum dot, which makes it possible to achieve selective ejection of a desired number of electrons.

This Chapter has been published in Applied Physics Letters **93**, 222103 (2008).

4.1 Introduction

Single-electron (SE) transfer and manipulation have been attracting much interest due to their potential applications to metrological current standards [1], SE circuits [2], charge qubits [3], SE sources [4], as well as single-photon sources [5]. In particular, the stringent criteria for the current standards require a nanoampere level current together with a transfer error of less than 10^{-8} to close the quantum metrological triangle through direct linking between ampere and frequency [6]. Inspired by the demonstration of SE pumps and turnstiles using multiple metal islands with fixed tunnel junctions [7, 8], the SE transfer in semiconductors has been extensively investigated toward the goal of higher-frequency operation by taking advantage of gate-induced tunable barriers or surface acoustic waves (SAWs) [9–12]. Recently, a simpler transfer scheme called the SE ratchet employing the modulation of a single barrier [13, 14] was demonstrated in a gigahertz frequency range to obtain a nanoampere level current. However, the transfer error is still large on the order of 10^{-2} [15], and the error mechanism in a tunable-barrier system is not fully understood. In general, the sources of the transfer error are the fluctuations in the electron number during the SE capture [13] as well as ejection into/from a quantum dot (QD). In order to open the route to a higher level of transfer accuracy, it is necessary to comprehend the dynamics of single electrons.

In this Chapter, we investigate the escape dynamics of electrons in the SE ratchet using Si nanowire metal-oxide-semiconductor field-effect transistors (MOSFETs). It is shown that the voltage-controlled ejection of single electrons can be achieved due to the Coulomb gap energy in the QD containing three electrons. Recently, the energy-dependent escape of a few electrons from SAW-defined dynamic QDs was observed on subnanosecond time scales [16]. We present here the direct time-resolved measurements of the characteristic times of the first, second, and third electrons to escape from the QD.

4.2 Experimental Details

Figure 4.1(a) shows a top-view scanning electron microscope image of the device. A 30 nm wide and thick Si nanowire is defined on a (001) silicon-on-insulator substrate with a 400 nm buried oxide by electron beam lithography. Thermal oxidation to form an approximately 20 nm thick gate oxide is followed by the formation of triple poly-Si gates. Subsequently, further thermal oxidation results in the gate width and the separation of approximately 10 nm and 100 nm, respectively. After the deposition of a 50 nm thick SiO_2, the entire region is covered with a wide poly-Si upper gate (UG), which is used as an implantation mask for the formation of n-type source and drain regions. When the voltage applied to UG ($V_{\rm UG}$) is positive, electrically induced source and drain are formed in the undoped silicon-on-insulator layers on both sides of the nanowire. For the operation of the single-electron transfer using the above device (device #1), an AC-pulse voltage ($V_{\rm G1}$) is applied to the source-side gate (G1) to form a time-modulated barrier in one-dimensional channel, while a steady barrier is formed underneath the center gate (G2) by a constant negative voltage ($V_{\rm G2}$). The drain-side gate is grounded throughout the experiments. When $V_{\rm G1}$ is switched from $V_{\rm G1H} = 0$ V (HIGH) to $V_{\rm G1L}$ (LOW), single electrons are captured from the source into the QD formed between G1 and G2 due to the Coulomb blockade [Fig. 4.1(b)]. Furthermore, the lift of the QD potential via the capacitive coupling between G1 and the QD leads to the ejection of the captured electrons over the G2 barrier to the drain. Thus, the periodic modulation of the asymmetric potential produces a rectified current of single electrons without any source-drain bias. When N electrons on average per cycle are conveyed from the source to the drain, the ratchet current, I, is quantized at Nef, where f is the clock frequency of the AC-pulse modulation. N is controlled predominantly using $V_{\rm UG}$ in order to deepen the QD potential during the SE capture. Figure 4.1(c) shows the ratchet current driven at $f = 16.7$ MHz as a function of $V_{\rm UG}$. The current plateaus are clearly observed corresponding to the discrete number of transferred electrons at 16 K. When $V_{\rm G1L}$ is -2.0 V, all captured electrons can be completely transferred to the drain. Figure 4.1(d) displays the contour plots of the

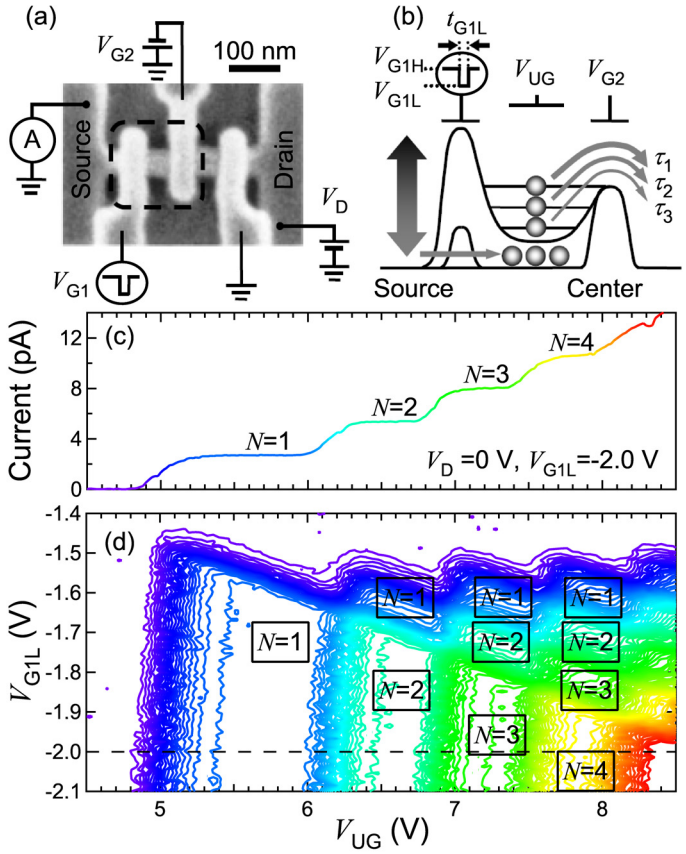

Figure 4.1: (a) Scanning electron microscope image of the Si nanowire device mounted with triple gates before the upper gate formation. (b) Schematic diagram of the SE ratchet employing the QD enclosed by the dashed line in the panel (a). (c) Quantization of the ratchet current observed at $V_{G2} = -1.0$ V. denotes the transferred electrons that are obtained by normalizing the ratchet current by ef. (d) Contour plots of the ratchet current as a function of V_{UG} and V_{G1L}. The iridescent curve shown in (c) corresponds to the scan along the dashed line in (d).

ratchet current as a function of V_{UG} and V_{G1L}. When V_{UG} is set to approximately 7.3 V, three electrons are prepared in the capture process. However, the number of actually transferred electrons is reduced from three to zero by making V_{G1L} less negative since the lift of the QD potential is not sufficient for the captured electrons to escape over the G2 barrier [13]. Namely, the less negative V_{G1L} results in an incomplete ejection of the single electrons, which motivates us to investigate their

escape dynamics.

4.3 Time-Resolved Measurements

We expect that the number of escaped electrons depends on the time length of the low state of the V_{G1L} pulse, t_{G1L}, since the surviving electrons tend to relax to the drain sooner or later. Therefore, we measure the average numbers of escaped electrons $\langle n_t \rangle = I/ef$ with varying of t_{G1L} at a constant time length of the high state of the V_{G1} pulse $t_{\mathrm{G1H}} = 10$ ns. The transfer operation is repeated about 10^6 times during the integration time for measuring the ratchet current. Figure 4.2(a) shows the time-resolved measurements of the escape of a few electrons from the bound states formed at a different V_{G1L}. The plateaus at $\langle n_t \rangle$ =1 and 2 are observed because of the incomplete SE ejection. Figure 4.2(b) shows a typical time-domain analysis at $V_{\mathrm{G1L}} = -1.796$ V. Intriguingly, the first and second electrons escape within 10 ns after applying the G1 low-state pulse whereas the third electron remains for a relatively longer duration.

In order to determine the escape times of the electrons, we compare the experimental results with an analytical solution obtained from the following master equations. The escape time, the average time before the n-th escape event to occur in one cycle, is defined as τ_n [see Fig. 4.1(b)], and the probability of m-electron survival in the QD is defined as $P_m(t_{\mathrm{G1L}})$. The master equations of the survival probability are expressed as $dP_m/dt_{\mathrm{G1L}} = P_{m+1}/\tau_n - P_m/\tau_{n+1}$ under the conditions of $n + m = 3$ and $P_3(0) = 1$ [17]. Hence, the average numbers of escaped electrons can be obtained as the following expectation $\langle n_t \rangle = \Sigma_{n,m} n P_m(t_{\mathrm{G1L}})$:

$$\begin{aligned}\langle n_t \rangle = 3 - \frac{1}{\tau_2 - \tau_1} \Bigg[& \left(\frac{\tau_3 \tau_1}{\tau_3 - \tau_1} + \tau_2 - 3\tau_1 \right) \exp\left(-t_{\mathrm{G1L}}/\tau_1\right) \\ & - \left(\frac{\tau_3 \tau_2}{\tau_3 - \tau_2} - 2\tau_2 \right) \exp\left(-t_{\mathrm{G1L}}/\tau_2\right) \\ & + \left(\frac{\tau_3 \tau_2}{\tau_3 - \tau_2} - \frac{\tau_3 \tau_1}{\tau_3 - \tau_1} \right) \exp\left(-t_{\mathrm{G1L}}/\tau_3\right) \Bigg]. \end{aligned} \tag{4.1}$$

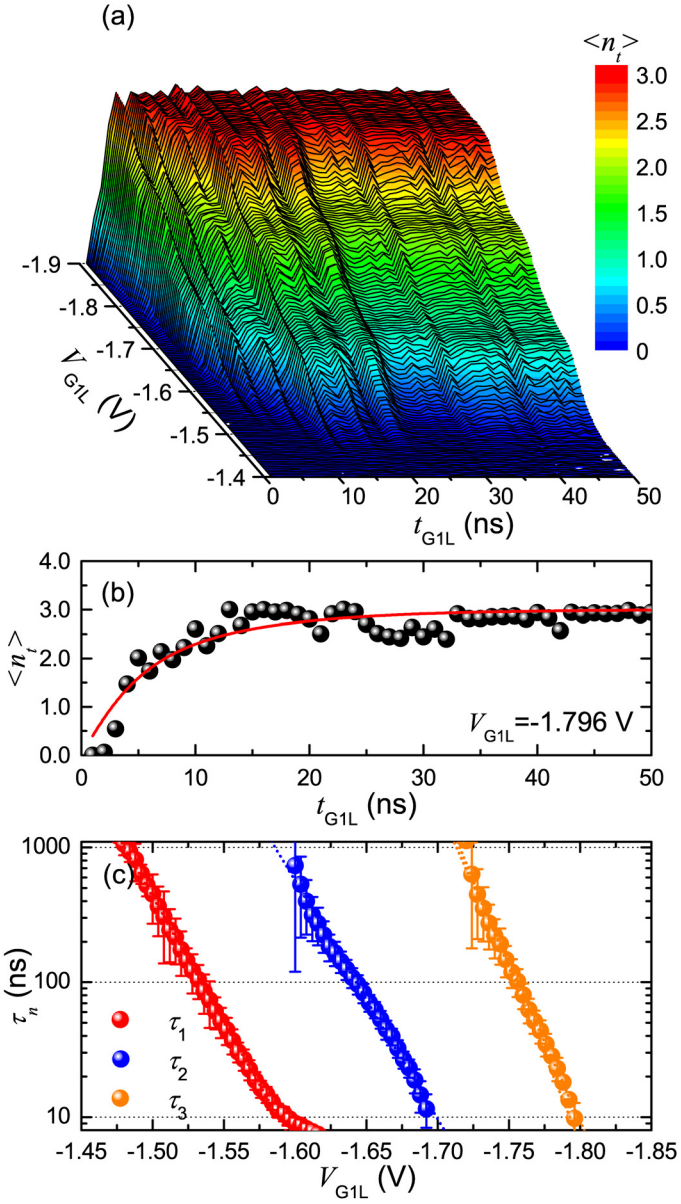

Figure 4.2: (a) Average number of escaped electrons as a function of t_{G1L} and V_{G1L}. (b) Typical time-domain analysis at $V_{\mathrm{G1L}} = -1.796$ V. (c) Exponential dependence of the escape time on V_{G1L}. The bars show the standard error included in the fitting routine.

We ignore the hopping back of the electrons from the drain over the high center barrier of ∼160 meV. As shown in Fig. 4.2(b), the theoretical curve is well fitted to the experimental results. Figure 4.2(c) plots the escape times determined as the fitting parameters. Each escape time is exponentially extended by making V_{G1L} less negative. Naturally, a large negative V_{G1L} is needed for the purpose of a high-speed SE transfer. In addition, it should be noted that the escape times become longer by more than one order of magnitude for the latter turn of the escape event. Such a number-selective ejection of single electrons is attributed to the SE charging effect in the QD. This is because the latter escaping electrons experience an additional energy barrier by the Coulomb gap energy.

4.4 Single-Electron Escape Process

The escape process can be explained by the classical thermal activation and/or quantum tunneling across a parabolic barrier since both can account for the exponential dependence of the escape time. Accordingly, we investigate the temperature dependence of escape rate Γ_n, which is the inverse of τ_n, in the temperature range between 16 K and 28 K [Fig. 4.3(a)]. Another device comprising a 40 nm wide Si nanowire (device #2) was measured at $V_{\mathrm{UG}} = 12.2$ V, where two electrons are initially bound within the QD. The slopes of Γ_1 and Γ_2 against V_{G1L} decrease as the temperature increases. In comparison to Fig. 4.3(b), this behavior is qualitatively consistent with the temperature-dependent current characteristic in the subthreshold regime of the MOSFET operated by G2. Therefore, we think the thermal activation rather than the tunneling [18] dominates the escape process of single electrons at the temperature around 16 K. As a result, the Coulomb gap energy between m and $m+1$ electron states can be estimated to be a several meV from $E_{Cm,m+1} = k_B T \ln(\tau_{n+1}/\tau_n)$, where k_B is the Boltzmann constant and T is the temperature.

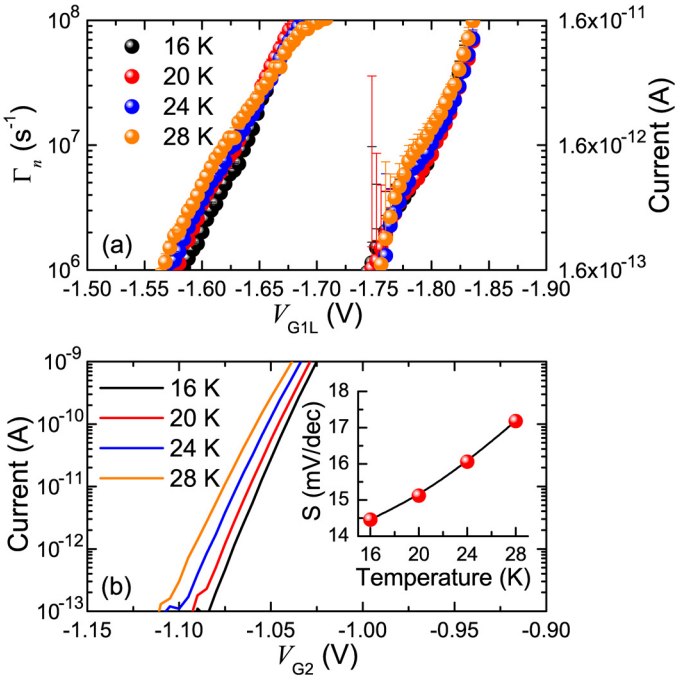

Figure 4.3: Temperature dependence of (a) escape rate in the SE ratchet and (b) currents in the subthreshold regime of the MOSFET operated by G2 at $V_{\mathrm{D}} = 100$ mV, which was measured using device #2. In the upper panel (a), two series of plots show Γ_1 and Γ_2 from the left, and the right-side axis indicates the relevant current values. The inset in (b) shows the subthreshold swing (S-factor).

4.5 Accuracy of Single-Electron Ejection

Based on the exponential dependence of the escape time, we can obtain $\langle n_t \rangle$ from Eq. (4.1) as a function of V_{G1L} [Fig. 4.4(a)]. The calculated $\langle n_t \rangle$ and its first derivative with respect to $|V_{\mathrm{G1L}}|$ reproduce the experimental results obtained using device #1. The transition regions between the plateaus have a finite slope, which results from the thermally fluctuating number of escaping electrons. We also estimate the ejection accuracy from the escape probability of n electrons p_n [Fig. 4.4(b)]. Here, p_n is equal to P_{3-n}. The asymmetric variation of p_n, more specifically a gradual rise and a sharp fall, reflects the peak shape in the first derivative curve shown in Fig. 4.4(a). This is derived from the electron-number dependence of the escape time.

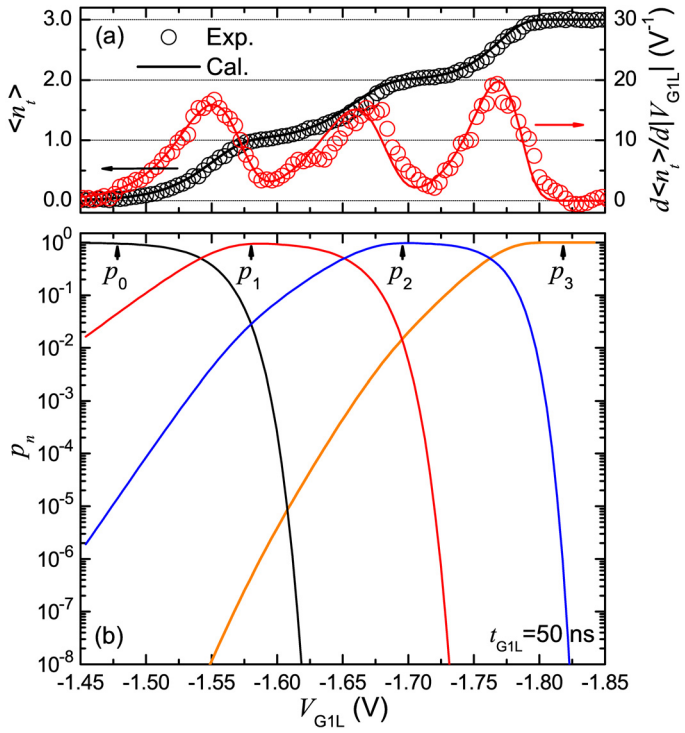

Figure 4.4: (a) Comparison of the experimental results obtained using device #1 with the calculated average number of escaped electrons and its first derivative with respect to $|V_{\mathrm{G1L}}|$. (b) Escape probability of n electrons as a function of V_{G1L}.

Moreover, p_n and p_{n+1} cross each other in the transition regions. Then, the ejection accuracy is the lowest. In contrast, p_{n-1} and p_{n+1} are suppressed on the plateaus, where the accuracy of n-electron ejection is maximized. Hence tuning of V_{G1L} allows us to achieve highly accurate ejection of a desired number of electrons. It should be added that the ejection error can drop below 10^{-8} by making V_{G1L} sufficiently negatively large, for example, much less than -1.8 V in Fig. 4.4(b).

4.6 Conclusions

In conclusion, we demonstrated the time-resolved measurements of the escape of a few electrons from the QD to determine both the escape times and the ejection accuracy in the SE ratchet. It was found that selective ejection of a desired number of electrons can be achieved by virtue of the SE charging effect in the QD. We believe

that the observed electron-number dependence of the escape time also plays a role in the capture process, and thereby the present findings are important for building a complete model of SE transfer.

References

[1] M. W. Keller, J. M. Martinis, N. M. Zimmerman, and A. H. Steinbach, Appl. Phys. Lett. **69**, 1804 (1996).

[2] K. Nishiguchi, Y. Ono, A. Fujiwara, H. Inokawa, and Y. Takahashi, Appl. Phys. Lett. **92**, 062105 (2008).

[3] T. Hayashi, T. Fujisawa, H. D. Cheong, Y. H. Jeong, and Y. Hirayama, Phys. Rev. Lett. **91**, 226804 (2003).

[4] F. Fève, A. Mahé, J.-M. Berroir, T. Kontos, B. Plaçais, D. C. Glattli, A. Cavanna, B. Etienne, and Y. Jin, Science **316**, 1169 (2007).

[5] J. Kim, O. Benson, H. Kan, and Y. Yamamoto, Nature (London) **397**, 500 (1999).

[6] R. E. Elmquist, N. M. Zimmerman, and W. H. Huber, IEEE Trans. Instrum. Meas. **52**, 590 (2003).

[7] M. H. Devoret, D. Esteve, and C. Urbina, Nature (London) **360**, 547 (1992).

[8] J. P. Pekola, J. J. Vartiainen, M. Möttänen, O.-P. Saira, M. Meschke, and D. V. Averin, Nature Phys. **4**, 120 (2008).

[9] L. P. Kouwenhoven, A. T. Johnson, N. C. van der Vaart, and C. J. P. M. Harmans, Phys. Rev. Lett. **67**, 1626 (1991).

[10] A. Fujiwara, N. M. Zimmerman, Y. Ono, and Y. Takahashi, Appl. Phys. Lett. **84**, 1323 (2004).

[11] M. D. Blumenthal, B. Kaestner, L. Li, S. Giblin, T. J. B. M. Janssen, M. Pepper, D. Anderson, G. Jones, and D. A. Ritchie, Nature Phys. **3**, 343 (2007).

[12] J. M. Shilton, V. I. Talyanskii, M. Pepper, D. A. Ritchie, J. E. F. Frost, C. J. B. Ford, C. G. Smith, and G. A. C. Jones, J. Phys.: Condens. Matter **8**, L531 (1996).

[13] A. Fujiwara, K. Nishiguchi, and Y. Ono, Appl. Phys. Lett. **92**, 042102 (2008).

[14] B. Kaestner, V. Kashcheyevs, S. Amakawa, M. D. Blumenthal, L. Li,

T. J. B. M. Janssen, G. Hein, K. Pierz, T. Weimann, U. Siegner, and H. W. Schumacher, Phys. Rev. B **77**, 153301 (2008).

[15] N. Maire, F. Hohls, B. Kaestner, K. Pierz, H. W. Schumacher, and R. J. Haug, Appl. Phys. Lett. **92**, 082112 (2008).

[16] M. R. Astley, M. Kataoka, C. J. B. Ford, C. H. W. Barnes, D. Anderson, G. A. C. Jones, I. Farrer, D. A. Ritchie, and M. Pepper, Phys. Rev. Lett. **99**, 156802 (2007).

[17] The assumption that three electrons are exactly bound within the QD is not true because the error involved in regard to the capture process causes the other neighboring states. However, the discussion does not change significantly even if a fraction of the capture error of $\sim 10^{-2}$ at the level of the transfer error is taken into account.

[18] H. Kawaura, T. Sakamoto, and T. Baba, Appl. Phys. Lett. **76**, 3810 (2000).

Chapter V

Resonant Escape over an Oscillating Barrier in Single-Electron Ratchet

Single-electron escape from a metastable state over an oscillating barrier is experimentally investigated in silicon-based ratchet transfer. When the barrier is oscillating on a time scale characteristic of the single-electron escape, synchronization occurs between the deterministic barrier modulation and the stochastic escape events. The average escape time as a function of its oscillation frequency exhibits a minimum providing a primary signature for resonant activation of single electrons.

This Chapter has been submitted to Physical Review B.

5.1 Introduction

When noise-induced hopping of a Brownian particle between two stable states is subject to weak periodic perturbation, stochastic resonance takes place as a cooperative phenomenon between the noise and signal [1]. Although the concept of stochastic resonance was originally propounded as a possible explanation for ice-age periodicity, it is currently observed in a wide spectrum of nonlinear dynamic systems such as electronic circuits [2], tunnel diodes [3], superconducting quantum interference devices (SQUIDs) [4], nanoelectromechanical systems (NEMS) [5], and semiconductor-based neural networks [6]. Over the past few decades, this phenomenon has received considerable attention in regard to potential applications to coherent signal amplifiers through the assistance of incoherent fluctuations that cannot be suppressed or eliminated. It was shown that such counterintuitive behavior is due to the matching between a deterministic time scale and a stochastic one, that is, the signal period and the hopping time, respectively [7, 8].

A large amount of theoretical work predicted an analogous phenomenon called resonant activation [9–19]. Particle escape from a potential well is driven when the potential barrier is oscillating on a time scale characteristic of the particle escape itself. For an oscillation frequency much lower than the order of the escape rate, the average escape time is the mean of the crossing times over each of the higher- and lower-state barriers. In the fast limit of the oscillation, the average escape time is the effective time required to cross the quasi-static barrier with average height. At an intermediate frequency, the average escape time resonantly takes a minimum. Until now, only the resonant escape of macroscopic variables has been observed in tunnel diodes [20] and current-biased Josephson junctions [21]. To actualize Brownian systems on a nanoscale, the alternative use of an electron as a classical particle has been considered [22]. In particular, explored based on the motivation for current standards with a metrological accuracy, single-electron ratchet transfer devices [23] provide us with a physical platform for investigating the nonequilibrium dynamics of single electrons in metastable states. Recently, we suggested that an intrinsic noise arising

from a thermal bath can play a significant role in single-electron ratchet transfer at 16 K [24]. By means of the same manner of transfer, we present here the experimental observation of single-electron resonant escape over an oscillating barrier.

5.2 Experimental Details

On a 400-nm buried oxide of a (001) silicon-on-insulator (SOI) wafer, a Si nanowire is lithographically defined with an approximate width of 30 nm and the thickness of 30 nm. After a 20 nm-thick thermal oxide film is formed on the nanowire, it is surrounded by triple poly-Si gates. Figure 5.1(a) displays the top-view scanning electron microscope image of the Si nanowire metal-oxide-semiconductor field-effect transistors (MOSFETs). Further thermal oxidation reduces the definite gate length to approximately 40 nm. A 50 nm-thick SiO_2 layer is deposited on the whole device region, which is followed by the formation of a poly-Si upper gate (UG). The wide UG layer is used as a mask during the ion implantation to form n-type contact areas. The application of a positive voltage to UG ($V_{\rm UG}$) accumulates electrons in the undoped SOI layers left underneath UG, thereby electrically inducing source and drain on both edges of the nanowire.

Prior to investigating the single-electron escape over the oscillating barrier, we describe the transfer scheme of the single-electron ratchet. Now, an applied voltage to the source-side gate (G1) is pulse-modulated between $V_{\rm G1H} = 0$ V and $V_{\rm G1L}$ at a fixed ratchet clock of $f_{\rm RC} = 16.67$ MHz while a constant voltage of $V_{\rm G2}$ is applied to the center gate (G2). The drain-side gate is grounded throughout this investigation. As shown in Fig. 5.1(b), a dynamic quantum dot formed between G1 and G2 captures single electrons from the source due to the Coulomb blockade. The number of captured electrons N can be controlled by $V_{\rm UG}$. By lifting the potential bottom sufficiently, the single electrons captured in a potential well can escape to the drain. Repetitive transfer of single electrons produces a quantized current of $I = Nef_{\rm RC}$ [23]. Figures 5.1(c)-(e) show the current staircases measured at 16 K as a function of $V_{\rm UG}$ and $V_{\rm G1L}$. The trapping of approximately one electron in each ratchet cycle can be thus brought about when $V_{\rm UG}$ is set to around 5.0 V [Fig. 5.1(d)].

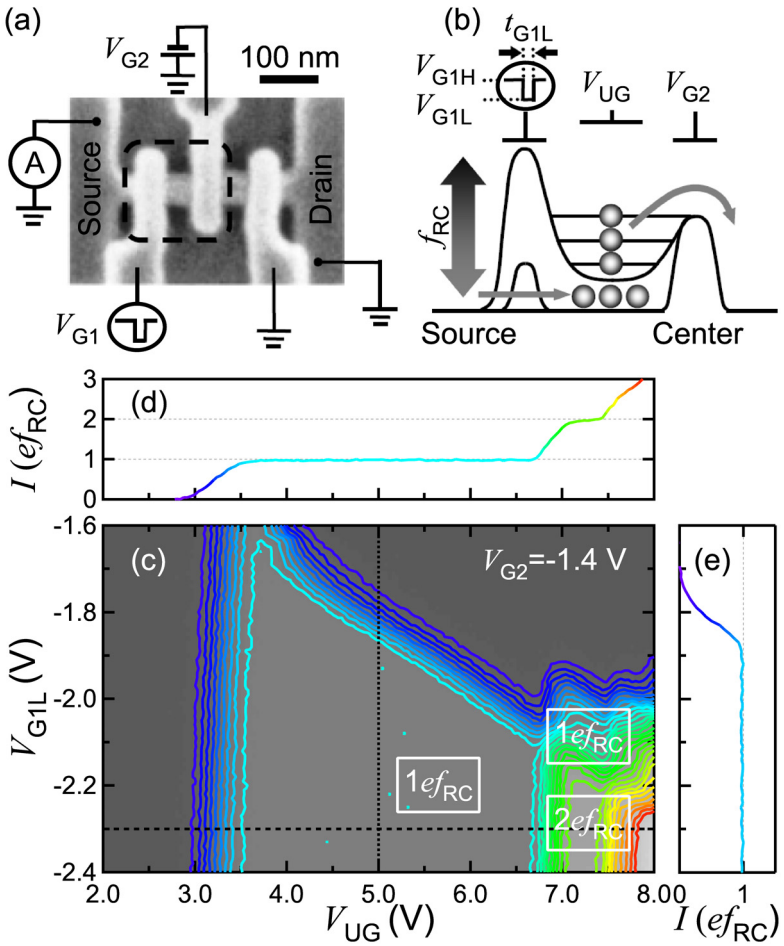

Figure 5.1: (a) Scanning electron microscope image of the Si nanowire device mounted with triple gates before the UG formation. (b) Schematic of the single-electron ratchet transfer employing a dynamic quantum dot enclosed by the dashed line in panel (a). (c) Contour plots of the transfer current I as a function of $V_{\rm UG}$ and $V_{\rm G1L}$. Contour lines are described every $0.1ef_{\rm RC}$ step. (d)(e) Quantized current staircases obtained by the scans along the horizontal and vertical lines in (c).

However, whether or not the captured single electrons actually escape and contribute to the current depends on the height of the potential bottom controlled by $V_{\rm G1L}$ [Fig. 5.1(e)]. Then the probability that single electrons escape from the metastable state $P_{\rm e}$ (less than one) can be calculated as a value of I normalized by $ef_{\rm RC}$. Since approximately 10^6 electrons are involved during the current integration, $P_{\rm e} = I/ef_{\rm RC}$

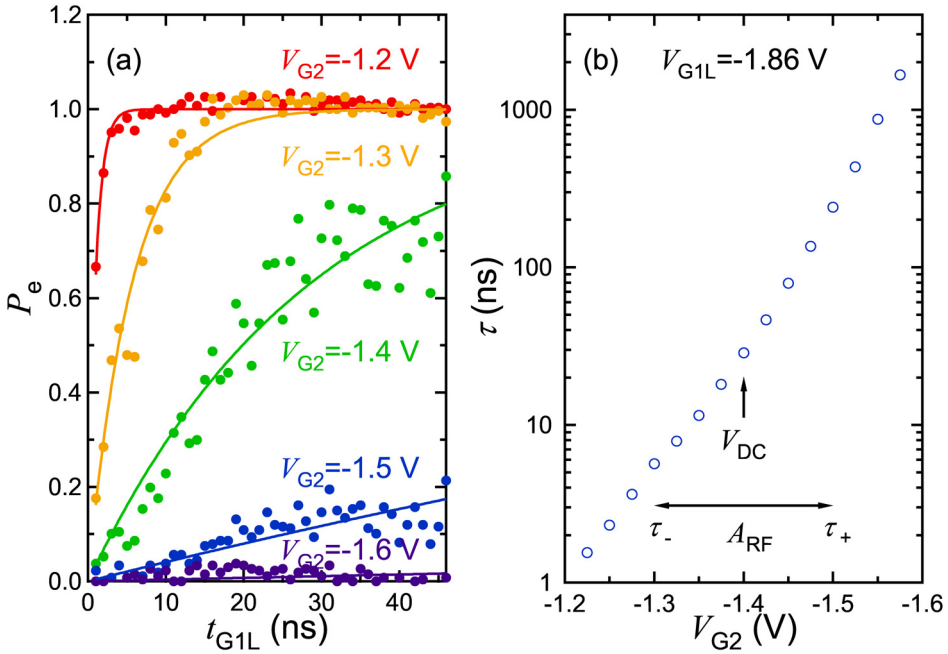

Figure 5.2: (a) Time evolutions of the probability of electrons escaping from the metastable state P_e recorded at typical values of V_{G2}. The experimental plots are fitted with single-exponential curves (solid lines), from which the escape times τ are determined. (b) Exponential dependence of τ on V_{G2} obtained at $V_{G1L} = -1.86$ V.

denotes a statistically averaged value. The time evolution of P_e can be monitored by changing the duration for which V_{G1L} is applied, t_{G1L}. Figure 5.2(a) shows the time-resolved results of P_e recorded at typical values of V_{G2}, which vary the height of the barrier underneath G2. Clearly, electron escape is more likely for the lower-height barriers. The escape time τ is determined by fitting the results with a single exponential curve. In Fig. 5.2(b), the obtained τ is plotted as a function of V_{G2}. Exponential dependence of τ on V_{G2} indicates that the escape dynamics are governed by the well-known Kramers' relation [25].

5.3 Dynamics of Single-Electron Escape over an Oscillating Barrier

In order to form a dichotomously oscillating barrier as illustrated in Fig. 5.3(a), V_{G2} is weakly modulated at the center of $V_{\mathrm{DC}} = -1.4$ V with a square-wave amplitude of $A_{\mathrm{RF}} = 200$ mV. The escape rate τ^{-1} is then in the order of 1 to 100 MHz [Fig. 5.2(b)]. When the RF frequency f_{RF} is changed within the range from 0.16 to 158.5 MHz [26], synchronization is anticipated to occur between the deterministic RF signal and the stochastic single-electron escape. Figure 5.3(b) shows that the current staircase observed in Fig. 5.1(e) is deformed by changing f_{RF}. It is clear that the escape behavior of electrons depends on the oscillating frequency of the barrier. A wide plateau of $P_{\mathrm{e}} \sim 0.5$ appears in a lower-frequency regime whereas in a higher-frequency regime the contour lines of $P_{\mathrm{e}} \geq 0.5$ are significantly pushed out towards a negatively smaller V_{G1L}, which indicates more efficient escape of single electrons.

The escape dynamics of single electrons over the oscillating barrier are highlighted through time-resolved measurements. Figure 5.4(a) shows the time-domain data of escaping electrons as a function of f_{RF} in contour plot form. Similar to the phenomena observed in Fig. 5.3(b), electron escape is suppressed in the lower-frequency regime whereas it is resonantly driven by the RF signal with the f_{RF} around several tens of megahertz. Here, the quantity of our central interest is the average escape time defined as $\tau_{\mathrm{avg}} = \int_0^\infty t_{\mathrm{G1L}} \left(-dP_{\mathrm{s}}/dt_{\mathrm{G1L}}\right) dt_{\mathrm{G1L}}$, where $P_{\mathrm{s}} = 1 - P_{\mathrm{e}}$ is the probability of electrons surviving in the potential well. For the low-frequency regime, the escaping electrons surmount the two-height barrier slowly oscillating between the higher and lower states with a 50-50 duty cycle [Fig. 5.3(c)]. The temporal evolution of P_{s} shown in Fig. 5.4(b) unambiguously exhibits the double-exponential decay at a low RF frequency of $f_{\mathrm{RF}} = 0.16$ MHz. Accordingly, P_{s} is approximately characterized by two different escape times τ_+^{RF} and τ_-^{RF} in the low-frequency regime: $P_{\mathrm{s}} = \left[\exp\left(-t_{\mathrm{G1L}}/\tau_+^{\mathrm{RF}}\right) + \exp\left(-t_{\mathrm{G1L}}/\tau_-^{\mathrm{RF}}\right)\right]/2$. Here τ_{avg} becomes identical to $\left(\tau_+^{\mathrm{RF}} + \tau_-^{\mathrm{RF}}\right)/2$. On the other hand, when f_{RF} is as high as the inverse of the time required for electron escape over the lower-state barrier τ_-^{-1}, single electrons

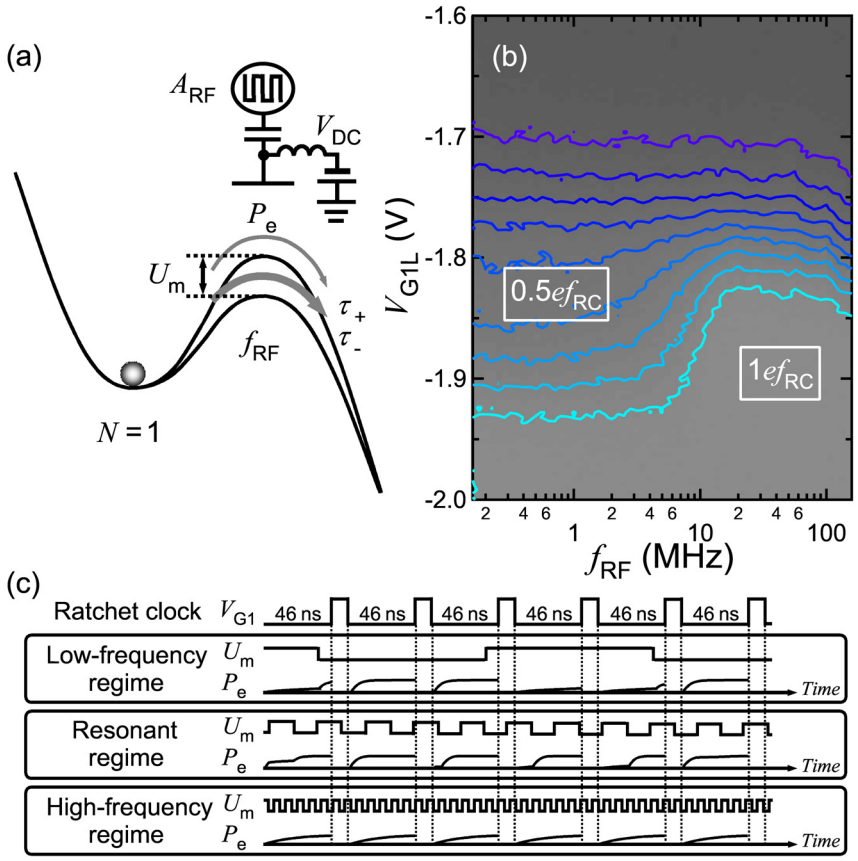

Figure 5.3: (a) Schematic of the single-electron escape over a barrier weakly modulated by the RF signal. (b) Contour plots of the transfer current I as a function of f_{RF} and V_{G1L}. Contour lines are described every $0.1ef_{\mathrm{RC}}$ step. (c) Time-sequence diagram of P_{e} response to the dichotomous barrier modulation U_{m} in low-frequency, resonant, and high-frequency regimes. Out of phase with the RF signal, the single-electron ratchet transfer is independently operated in the ratchet clock period of $f_{\mathrm{RC}}^{-1} = 60$ ns.

preferentially cross the lower-state barrier at least once [Fig. 5.3(c)]. For a very high f_{RF}, single electrons experience an average-height barrier. In these higher-frequency regimes, P_{s} likely represents a single-exponential decay of $P_{\mathrm{s}} = \exp\left(-t_{\mathrm{G1L}}/\tau^{\mathrm{RF}}\right)$ [Fig. 5.4(b)]. τ_{avg} is then given by τ^{RF}. Thus, τ_{avg} can be obtained with good approximation by means of single- or double-exponential fitting. In Fig. 5.4(c), τ_{avg} is plotted as a function of f_{RF}. As expected, τ_{avg} is found to manifest a resonance. Such a nonmonotonic feature is robust and can be observed even when the order of τ_{avg} is

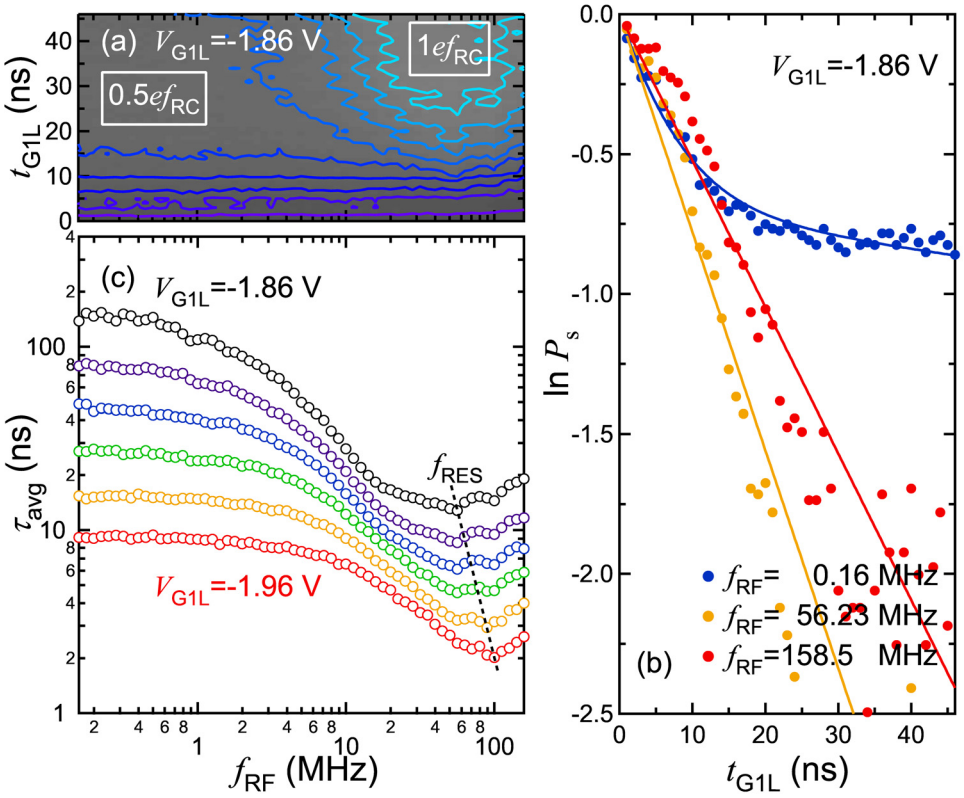

Figure 5.4: (a) Contour plots of the transfer current I as a function of f_{RF} and t_{G1L}. Contour lines are described every $0.1ef_{\mathrm{RC}}$ step. (b) Temporally decaying probability of electrons surviving in the potential well $P_{\mathrm{s}} = 1 - P_{\mathrm{e}}$ measured at low, resonant, and high frequencies. The solid lines are given by fitting with the single- or double-exponential functions. (c) RF-frequency dependence of the average escape time τ_{avg} obtained at different values of V_{G1L}. The dotted line indicates a correlation between the minimum values of τ_{avg} and the resonant frequencies f_{RES}.

changed by V_{G1L}. The resonant frequency f_{RES} exhibits a shift to higher frequencies for a shorter τ_{avg} and furthermore the minimum τ_{avg} at f_{RES} is shifted along the dotted line. Namely, the time-scale matching with the deterministic barrier modulation triggers the stochastic single-electron emission. It is worth emphasizing that the observed phenomenon is clearly distinguished from the photon-assisted tunneling that can be observed when the photon energy matches or exceeds the separation between discrete levels in the potential well [27].

5.4 RF-Amplitude Dependence

In addition, the resonant variation of $\tau_{\rm avg}$ can be tuned by $A_{\rm RF}$ as shown in Fig. 5.5(a). With an increase in $A_{\rm RF}$, the differences in $\tau_{\rm avg}$ between the lower- and higher-frequency regimes become more pronounced with the inflection points clamped around 8 MHz where $\tau_{\rm avg}$ is almost the same as the value of τ at $V_{\rm DC}$ [Fig. 5.2(b)] [17]. The experimental results are compared with the kinetic approximation [19], which is a theoretical framework effective only for a frequency regime lower than $f_{\rm RES}$. Equation (58) in Ref. 19 is given as

$$\tau_{\rm kin} = \frac{1}{2}\left(\tau_+ + \tau_-\right) - \frac{1}{2}\left(\tau_+ - \tau_-\right)\frac{q_+ - q_-}{1 - q_+ q_-}, \tag{5.1}$$

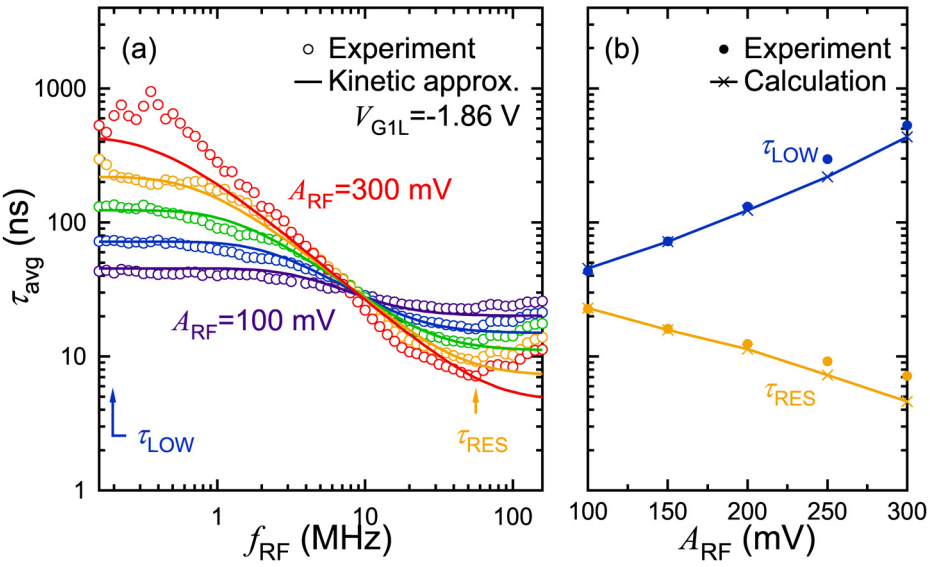

Figure 5.5: (a) Comparison of the resonant behaviors observed as increasing the RF amplitude $A_{\rm RF}$ with the kinetic approximation given by Eq. (5.1). $\tau_{\rm LOW}$ and $\tau_{\rm RES}$ are $\tau_{\rm avg}$ obtained at the low-frequency limit in the present experiment and at the resonant frequency, respectively. (b) Variations in $\tau_{\rm LOW}$ and $\tau_{\rm RES}$ as a function of $A_{\rm RF}$. The two values are respectively compared to $\tau_{\rm kin}|_{f_{\rm RF}\to 0} = (\tau_+ + \tau_-)/2$ (upper solid line) and $\tau_{\rm kin}|_{f_{\rm RF}\to\infty} \approx 2\tau_-$ (lower solid line).

where $q_{\pm} = \exp(-1/2\tau_{\pm} f_{\mathrm{RC}})$. In Fig. 5.5(a) the results of the kinetic approximation are plotted, which are calculated based on Eq. (5.1) using τ_+ and τ_- estimated from Fig. 5.2(b). Good agreements with the kinetic approximation are obtained except for a frequency regime higher than f_{RES} [28]. In the high-frequency regime where single electrons surmount the average-height barrier, τ_{avg} should asymptotically approach an A_{RF}-independent value of $\sqrt{\tau_+\tau_-}$ predicted by resonant activation theory [9], which is equal τ at V_{DC} in Fig. 5.2(b). In the present experiment, it is confirmed that τ_{avg} in the high-frequency regime gradually deviates from τ_{kin} and exhibits a slight increase as expected.

Finally, we discuss the physical meanings of τ_{LOW} and τ_{RES} extracted from Fig. 5.5(a) by comparing them to the limit values of τ_{kin} in Fig. 5.5(b). τ_{LOW} is consistent with $\tau_{\mathrm{kin}}|_{f_{\mathrm{RF}}\to 0} = (\tau_+ + \tau_-)/2$. In this limit electron escape takes place over either the higher-state barrier or lower-state barrier exclusively with probability 1/2 for each. Especially when $\tau_- < t_{\mathrm{G1L}} < \tau_+$, electron escape is almost suppressed for the higher-state barrier, thereby giving rise to 0.5 plateaus in Figs. 5.3(b) and 5.4(a). Meanwhile, τ_{RES} is well approximated by $\tau_{\mathrm{kin}}|_{f_{\mathrm{RF}}\to\infty} = 2/(\tau_+^{-1} + \tau_-^{-1}) \approx 2\tau_-$. This implies that the escaping electrons most likely cross the barrier when it is switched to the lower state [9]. More specifically, even if single electrons once fail to cross the lower-state barrier, they have another chance after a half period of f_{RF}^{-1}. Hence, the quantitative evaluation supports that the observed phenomenon can be intuitively understood as shown in Fig. 5.3(c).

5.5 Conclusions

In conclusion, the stochastic resonant escape of a Brownian particle on a nanoscale was demonstrated by using silicon-based single-electron ratchet transfer. The non-monotonic behavior was observed for the transfer current in response to the weak barrier modulation, which was verified by comparing the resonant variations of the average escape times with the kinetic approximation. For the barrier-oscillating frequency low compared to the escape rate, the transfer current is suppressed since single electrons are inevitably subject to the higher-state barrier formed with probability

1/2. When the barrier is oscillating at a frequency in the order of τ_-, the majority of the escape events take place in the configuration of the lower-state barrier. The strong correlation in the characteristic time scales induces the resonant escape of single electrons, consequently enhancing the transfer current. The expected tendency to approach a constant value in the high frequency regime manifests as the deviation from the kinetic approximation. The physical origin of the observed phenomenon is the stochastic resonance in the single-electron system showing that the periodically controlled barrier modulation can synchronize with the temporally fluctuated ejection of single electrons. The understanding of such a coordinated interaction between the deterministic signal and the stochastic events would be of importance for highly accurate and noise-robust operation of single-electron devices nonisolated from a thermal bath.

References

[1] For a review, see K. Wiesenfeld and F. Moss, Nature (London) **373**, 33 (1995); A. R. Bulsara and L. Gammaitoni, Phys. Today **49**(3), 39 (1996); L. Gammaitoni, P. Hänggi, P. Jung, and F. Marchesoni, Rev. Mod. Phys. **70**, 223 (1998).

[2] S. Fauve and F. Heslot, Phys. Lett. A **97**, 5 (1983); K. Murali, S. Sinha, W. L. Ditto, and A. R. Bulsara, Phys. Rev. Lett. **102**, 104101 (2009).

[3] R. N. Mantegna and B. Spagnolo, Phys. Rev. E **49**, R1792 (1994).

[4] R. Rouse, S. Han, and J. E. Lukens, Appl. Phys. Lett. **66**, 108 (1995); A. D. Hibbs, A. L. Singsaas, E. W. Jacobs, A. R. Bulsara, J. J. Bekkedahl, and F. Moss, J. Appl. Phys. **77**, 2582 (1995).

[5] R. L. Badzey and P. Mohanty, Nature (London) **437**, 995 (2005).

[6] S. Kasai and T. Asai, Appl. Phys. Express **1**, 083001 (2008); A. Samardak, A. Nogaret, N. B. Janson, A. G. Balanov, I. Farrer, and D. A. Ritchie, Phys. Rev. Lett. **102**, 226802 (2009).

[7] L. Gammaitoni, F. Marchesoni, and S. Santucci, Phys. Rev. Lett. **74**, 1052 (1995).

[8] G. Giacomelli, F. Marin, and I. Rabbiosi, Phys. Rev. Lett. **82**, 675 (1999).

[9] C. R. Doering and J. C. Gadoua, Phys. Rev. Lett. **69**, 2318 (1992).

[10] U. Zürcher and C. R. Doering, Phys. Rev. E **47**, 3862 (1993).

[11] C. Van den Broeck, Phys. Rev. E **47**, 4579 (1993).

[12] M. Bier and R. D. Astumian, Phys. Rev. Lett. **71**, 1649 (1993); Phys. Lett. A **247**, 385 (1998).

[13] J. J. Brey and J. Casado-Pascual, Phys. Rev. E **50**, 116 (1994).

[14] P. Pechukas and P. Hänggi, Phys. Rev. Lett. **73**, 2772 (1994).

[15] P. Hänggi, Chem. Phys. **180**, 157 (1994).

[16] P. Reimann, Phys. Rev. Lett. **74**, 4576 (1995).

[17] M. Marchi, F. Marchesoni, L. Gammaitoni, E. Menichella-Saetta, and S. Santucci, Phys. Rev. E **54**, 3479 (1996).

[18] J. Iwaniszewski, Phys. Rev. E **54**, 3173 (1996).

[19] M. Boguñá, J. M. Porrà, J. Masoliver, and K. Lindenberg, Phys. Rev. E **57**, 3990 (1998).

[20] R. N. Mantegna and B. Spagnolo, Phys. Rev. Lett. **84**, 3025 (2000).

[21] Y. Yu and S. Han, Phys. Rev. Lett. **91**, 127003 (2003).

[22] J. Maddox, Nature (London) **359**, 771 (1992); P. Hänggi and F. Marchesoni, Rev. Mod. Phys. **81**, 387 (2009).

[23] A. Fujiwara, K. Nishiguchi, and Y. Ono, Appl. Phys. Lett. **92**, 042102 (2008); B. Kaestner, V. Kashcheyevs, S. Amakawa, M. D. Blumenthal, L. Li, T. J. B. M. Janssen, G. Hein, K. Pierz, T. Weimann, U. Siegner, and H. W. Schumacher, Phys. Rev. B **77**, 153301 (2008).

[24] S. Miyamoto, K. Nishiguchi, Y. Ono, K. M. Itoh, and A. Fujiwara, Appl. Phys. Lett. **93**, 222103 (2008).

[25] P. Hänggi, P. Talkner, and M. Borkovec, Rev. Mod. Phys. **62**, 251 (1990).

[26] Initialization of single-electron trapping from the source is robust with respect to the continuous RF signal.

[27] T. H. Oosterkamp, L. P. Kouwenhoven, A. E. A. Koolen, N. C. van der Vaart, and C. J. P. M. Harmans, Phys. Rev. Lett. **78**, 1536 (1997).

[28] The fractional deviation in the low-frequency regime is mainly due to the double-exponential fitting within the finite measurement window.

Summary

This thesis described a wide range of phenomena from self-organization, quantum-mechanical effect, ratchet process, and stochastic effect occurring in group-IV semiconductor quantum dots; bottom-up Ge/Si quantum dots grown via the Stranski-Krastnov (SK) mode and top-down Si quantum dots based on silicon nanowire metal-oxide-semiconductor field-effect transistors (MOSFETs).

In Chapter II, I investigated atomic diffusion phenomena during nucleation and growth of Ge/Si nanoislands. In order to test the validity of the capture zone model where deposited adatoms were to be incorporated into the neighboring islands, a statistical assessment of the Voronoi cell analysis was introduced. The correlation between the grown island volumes and corresponding Voronoi cell areas provided a quantitative indicator and showed that the deposited Ge adatoms were not necessarily incorporated into the nearest neighboring islands. Further scaling analysis of the Voronoi cell areas enabled the determination of the atomic number required for a nucleus to be stable on the 2D layer. The experimentally obtained value was found to be even smaller than the subcritical nucleus size previously observed at a lower temperature. As a possible explanation for this, I suggested that the Si atoms incorporated from the alloyed 2D layer thermally stabilizes such small-size nuclei. This hypothesis was thereafter confirmed by the Raman analysis combined with ^{76}Ge isotope tracing; the incorporation of SiGe materials from the 2D layer encourages nucleation immediately after the 2D-3D transition. Additionally, it was found that a large portion of the 2D layer was decomposed in the end and the underlying Si substrate was exposed on the topmost surface. By investigations of the spatial correlation and internal strain, I also revealed that the strain-driven atomic diffusion took place between the strained pyramids and the adjacent relaxed domes even in the steady-state regime of the nucleation.

In Chapter III, I presented the Aharonov-Bohm (AB) effect on magnetoexcitons in isotopically pure ^{70}Ge/Si self-assembled type-II quantum dots. I paid particular attention to the sample preparation for suppressing nonradiative processes in order to obtain the optimal condition of excitation power for observing the excitonic AB effect. Low-temperature photoluminescence (PL) measurements were carried out with applying magnetic fields up to 5 T. The periodical oscillation of the PL intensity which was in phase with that of the peak energy was observed as a function of the magnetic fields. This was attributed to a process that the penetration of quantum flux through the electron ringlike trajectory induced the change in the angular momentum of a ground-state exciton. By taking this account into the modulation in the electron-hole overlap, I provided a qualitative interpretation for the oscillatory behavior of the PL intensity. Although more quantitative consideration of the observed phenomenon would be helpful, these results evidenced the phase coherence of an electron wave function localized in silicon. It will be interesting to investigate the AB phase due to ^{29}Si or ^{73}Ge nuclear spin fields in the future.

In Chapter IV, I investigated the escape dynamics of a few electrons in the single-electron ratchet based on silicon nanowire MOSFETs. Time-resolved measurements allowed me to determine their escape times in a nanosecond regime. The temperature dependence on the escape time showed that the thermal activation rather than quantum-tunneling process dominated the single-electron escape dynamics within the temperature range I investigated. In addition, the accuracy of single-electron ejection was evaluated in the single-electron ratchet transfer. All single electrons once trapped in the potential well could be ejected by sufficiently lifting the potential bottom. This indicates that the single-barrier modulation has a great advantage in the single-electron ratchet transfer. Further enhancement of the charging energy in the dynamic quantum dots is necessary to achieve the number-selective ejection with higher accuracy. These findings contribute to build a time-dependent model of single-electron transfer.

In Chapter V, I showed that periodical oscillations of barrier on a time scale characteristic of the stochastic escape process drove the resonant escape of single electrons. In the past, the experimental investigation of the behavior of an electron as

a Brownian particle was hardly dealt because of the difficulty in working with single electrons at high temperature. This limitation was overcome by the silicon-based single-electron ratchet transfer devices fabricated in this study. The physical origin of the phenomenon observed was interpreted in the same framework as the notion of the stochastic resonance. In other words, this experiment suggested the importance of the coordinated interaction between the stochastic single-electron behavior and the deterministic driving force. These findings will lead to a reliable operation of single-electron devices in the presence of intrinsic fluctuations such as thermal noise. For the further improvement of the transfer accuracy in the single-electron ratchet process, it is necessary to elucidate behaviors of the resonant escape of single electrons when a few electrons are contained in the potential. Although the stochastic resonance discussed in this thesis was limited to the classical regime, it is of interest to explore the quantum regime from the viewpoint of fundamental physics.

In order to balance the high controllability and high productivity in the fabrication of semiconductor quantum dot structures, it is indispensable to figure out the self-organization phenomenon. Furthermore, an understanding of both quantum phenomenon and fluctuation effects pronounced in nanostructures is necessary for realization of silicon quantum information processing. The physical phenomena found in the present thesis is therefore of importance for the operation design of future nanodevices.

Satoru Miyamoto
February 2010

List of Publications

[Journal Articles]

1. *Atomic transport in strain-mediated self-assembly studied by germanium stable isotopes*
   O. Moutanabbir, S. Miyamoto, E. E. Haller, and K. M. Itoh, Physical Review Letters (submitted).

2. *Resonant escape over an oscillating barrier in single-electron ratchet transfer*
   S. Miyamoto, K. Nishiguchi, Y. Ono, K. M. Itoh, and A. Fujiwara, Physical Review B (submitted).

3. *Evidence of magneto-exciton Aharonov-Bohm effect in nuclear-spin-free Ge/Si self-assembled type-II quantum dots*
   S. Miyamoto, O. Moutanabbir, T. Ishikawa, K. Sawano, Y. Shiraki, E. E. Haller, and K. M. Itoh, Physical Review Letters (submitted).

4. *Spatial correlation of self-assembled isotopically pure Ge/Si(001) nanoislands*
   S. Miyamoto, O. Moutanabbir, E. E. Haller, and K. M. Itoh, Physical Review B **79**, 165415 (2009); Selected for the April 20, 2009 issue of Virtual Journal of Nanoscale Science & Technology.

5. *Escape dynamics of a few electrons in a single-electron ratchet using silicon nanowire metal-oxide-semiconductor field-effect transistor*
   S. Miyamoto, K. Nishiguchi, Y. Ono, K. M. Itoh, and A. Fujiwara, Applied Physics Letters **93**, 222103 (2008).

6. *Tuning the luminescence emission of {105}-faceted Ge QDs superlattice using proton implantation and thermal annealing*
   O. Moutanabbir, S. Miyamoto, A. Sagara, H. Oshikawa, and K. M. Itoh, Thin Solid Films **517**, 391 (2008).

7. *Isotopically controlled self-assembled Ge/Si nanostructures*
   O. Moutanabbir, S. Miyamoto, A. Fujimoto, and K. M. Itoh, Journal of Crystal

Growth, **301-302**, 324 (2007).

[International Conferences]

1. *Room-temperature observation of quantum size effects in photoluminescence of $Si/Si_{0.8}Ge_{0.2}$ nanocolumns prepared by neutral beam etching*
   R. Hirano, S. Miyamoto, M. Yonemoto, S. Samukawa, K. Sawano, Y. Shiraki, and K. M. Itoh, International Symposium on Quantum Nanophotonics and Nanoelectronics 2009, November 18-20, 2009, Tokyo, Japan.

2. *Single-electron stochastic resonance using Si nano-wire transistors*
   K. Nishiguchi, S. Miyamoto, and A. Fujiwara, 22nd International Microprocesses and Nanotechnology Conference, November 16-19, 2009, Sapporo, Japan.

3. *Single-electron activation over an oscillating barrier in silicon nanowire MOSFETs*
   S. Miyamoto, K. Nishiguchi, Y. Ono, K. M. Itoh, and A. Fujiwara, 18th International Conference on Electronic Properties of Two-Dimensional Systems, July 19-24, 2009, Kobe, Japan.

4. *Nucleation and mass transport in strain-driven islanding studied by combination of Voronoi tessellation and Ge enriched isotope*
   S. Miyamoto, O. Moutanabbir, E. E. Haller, and K. M. Itoh, 6th International Conference on Silicon Epitaxy and Heterostructures, May 17-22, 2009, Los Angeles, USA.

5. *Escape dynamics of electrons in a single-electron ratchet using silicon nanowire MOSFETs*
   S. Miyamoto, K. Nishiguchi, Y. Ono, K. M. Itoh, and A. Fujiwara, 2nd IEEE Nanotechnology Materials and Device Conference, October 20-22, 2008, Kyoto, Japan.

6. *Dynamics of single-electron capture in Si nanowire MOSFETs*
   A. Fujiwara, S. Miyamoto, K. Nishiguchi, Y. Ono, and N. M. Zimmerman, 2008 IEEE Silicon Nanoelectronics Workshop, June 15-16, 2008, Honolulu, USA

7. *Anomalous x-ray scattering 3D mapping of strain and composition of Ge/Si shrinking islands during the initial stage of Si overgrowth*
   O. Moutanabbir, T. Kawamura, S. Miyamoto, S. Kimura, M. Mizumaki, and K. M. Itoh, 5th International Conference on Silicon Epitaxy and Heterostructures,

May 20-25, 2007, Marseille, France.

8. *Tuning the luminescence emission of {105}-faceted Ge QDs superlattice using proton implantation and thermal annealing*
   O. Moutanabbir, A. Sagara, S. Miyamoto, H. Oshikawa, and K. M. Itoh, 5th International Conference on Silicon Epitaxy and Heterostructures, May 20-25, 2007, Marseille, France.

9. *Artificial manipulation of the isotopic composition of Ge-Si epitaxial nanostructures*
   O. Moutanabbir, S. Miyamoto, and K. M. Itoh, 5th International Conference on Silicon Epitaxy and Heterostructures, May 20-25, 2007, Marseille, France.

10. *Subtleties in the epitaxial growth of Ge/Si nanstructures revealed by Raman scattering in combination with stable isotopes tracing*
    O. Moutanabbir, S. Miyamoto, and K. M. Itoh, 2nd International WorkShop on New Group IV Semiconductor Nanoelectronics, October 2-3, 2006, Sendai, Japan.

11. *Isotopically controlled self-assembled Ge/Si nanostructures*
    O. Moutanabbir, S. Miyamoto, A. Fujimoto, and K. M. Itoh, 14th International Conference on Molecular Beam Epitaxy, September 3-8, 2006,Tokyo, Japan.

12. *Pure germanium isotopes for investigation interdiffusion in uncapped self-assembled Ge/Si nanostructures*
    O. Moutanabbir, S. Miyamoto, Y. Tabuchi, and K. M. Itoh, 2006 Material Research Society Spring Meeting, April 17-21, 2006, San Francisco, USA.

[Domestic Conferences]

1. シリコン単電子ラチェット転送における振動ポテンシャル障壁を越える共鳴活性化現象
   宮本 聡, 西口 克彦, 小野 行徳, 伊藤 公平, 藤原 聡, 2009 年秋季 第 70 回応用物理学会学術講演会, 9 月 8 日-11 日, 2009, 富山大学

2. シリコン単電子ラチェット転送における少数電子脱出ダイナミクス
   宮本 聡, 西口 克彦, 小野 行徳, 伊藤 公平, 藤原 聡, 先端融合 COE「ナノ量子情報エレクトロニクス連携拠点」公開シンポジウム, 4 月 22 日, 2009, 東京大学

3. シリコン細線 MOSFET における単電子捕獲のダイナミクス

藤原 聡, 宮本 聡, 西口 克彦, 小野 行徳, N. M. Zimmerman, 2008 年秋季 第 69 回応用物理学会学術講演会, 9 月 2 日-5 日, 2008, 中部大学

4. シリコン細線 MOSFET を用いた単電子ラチェットにおける電子ダイナミクス
   宮本 聡, 西口 克彦, 小野 行徳, 藤原 聡, 伊藤 公平, 2008 年春季 第 55 回応用物理学関係連合講演会, 3 月 27 日-30 日, 2008, 日本大学理工学部

5. 無損傷中性粒子ビームエッチングを用いた SiGe 量子ナノディスク積層構造の作製 2
   米元 雅浩, 宮本 聡, 平野 梨伊, 澤野 憲太郎, 伊藤 公平, 白木 靖寛, 寒川 誠二, 2007 年秋季 第 68 回応用物理学関係連合講演会, 9 月 4 日-8 日, 2007, 北海道工業大学

6. 無損傷中性粒子ビーム加工を用いた SiGe 量子ナノディスク積層構造の作製
   齋藤 卓, 米元 雅浩, 相良 暁彦, 宮本 聡, 澤野 憲太郎, 伊藤 公平, 白木 靖寛, 寒川 誠二, 2007 年春季 第 54 回応用物理学関係連合講演会, 3 月 27 日-30 日, 2007, 青山学院大学.

7. 同位体制御 Ge/Si(001) ナノ構造における原子組成の定量評価
   宮本 聡, Oussama Moutanabbir, 伊藤 公平, 2007 年春季 第 54 回応用物理学関係連合講演会, 3 月 27 日-30 日, 2007, 青山学院大学.